nature communications

Article

https://doi.org/10.1038/s41467-025-56097-1

Microglial NLRP3-gasdermin D activation impairs blood-brain barrier integrity through interleukin-1β-independent neutrophil chemotaxis upon peripheral inflammation in mice

Received: 9 April 2024

Accepted: 9 January 2025

Published online: 15 January 2025

Check for updates

Sung-Hyun Yoon[1,7], Chae youn Kim[2,7], Eunju Lee[1,6], Changjun Lee[1], Kyung-Seo Lee[1], Jaeho Lee[3], Hana Park[4], Bokeum Choi[1], Inhwa Hwang[1], Junhan Kim[2], Tae-Gyun Kim[5], Junghyun Son[4], Young-Min Hyun[3], Seunghee Hong[2] ✉ & Je-Wook Yu[1] ✉

Blood-brain barrier (BBB) disintegration is a key contributor to neuroinflammation; however, the biological processes governing BBB permeability under physiological conditions remain unclear. Here, we investigate the role of NLRP3 inflammasome in BBB disruption following peripheral inflammatory challenges. Repeated intraperitoneal lipopolysaccharide administration causes NLRP3-dependent BBB permeabilization and myeloid cell infiltration into the brain. Using a mouse model with cell-specific hyperactivation of NLRP3, we identify microglial NLRP3 activation as essential for peripheral inflammation-induced BBB disruption. Conversely, NLRP3 and microglial gasdermin D (GSDMD) deficiency markedly attenuates lipopolysaccharide-induced BBB breakdown. Notably, IL-1β is not required for NLRP3-GSDMD-mediated BBB disruption. Instead, microglial NLRP3-GSDMD axis upregulates CXCL chemokines and matrix metalloproteinases around BBB via producing GDF-15, promoting the recruitment of CXCR2-containing neutrophils. Inhibition of neutrophil infiltration and matrix metalloproteinase activity significantly reduces NLRP3-mediated BBB impairment. Collectively, these findings reveal the important role of NLRP3-driven chemokine production in BBB disintegration, suggesting potential therapeutic targets to mitigate neuroinflammation.

The blood-brain barrier (BBB) is a specialized vascular structure in the brain consisting of multiple layers of endothelial cells, pericytes, and astrocytes[1]. It physically separates the brain parenchyma from the circulating blood, thereby preventing the entry of blood-borne toxic substances and circulating immune cells[2]. However, the BBB facilitates the selective transport of nutrients, ions, and water into the brain, contributing to brain homeostasis[3]. Dysfunction of the BBB is solely considered an outcome of various brain pathological conditions, including ischemic stroke[4]. When the BBB is compromised, a notable influx of circulating immune cells into the brain parenchyma occurs,

A full list of affiliations appears at the end of the paper. ✉e-mail: seungheehong@yonsei.ac.kr; jewookyu@yuhs.ac

leading to considerable inflammation[5]. Consequently, BBB disruption can exacerbate the pathological conditions of neurological diseases and is recognized as a potential risk factor for various neurodegenerative disorders[6].

Maintaining BBB integrity is crucial for preserving brain function homeostasis. Notably, BBB dysfunction is linked to vascular disorders such as stroke and multiple neurological disorders such as Parkinson's disease, Alzheimer's disease, epilepsy, and brain tumors[6–8]. Furthermore, recent studies demonstrated that systemic or peripheral inflammation resulting from COVID-19[9–11] or sepsis[12] can impair BBB integrity leading to the subsequent neuroinflammation[13,14]. However, the precise mechanisms underlying the regulation of BBB permeability in response to various pathological conditions, including peripheral inflammation, remain largely unknown.

Upon sensing diverse infection- or tissue injury-derived factors, NLRP3 triggers the assembly of inflammasome complex in the cytosol of myeloid cells, which in turn induces the subsequent activation and secretion of interleukin (IL)-1β, which plays a pivotal role in the initiation and propagation of inflammation[15,16]. Of interest, deregulated NLRP3 inflammasome activation significantly contributes to the pathogenesis of multiple neurological diseases such as Alzheimer's and Parkinson's diseases[17–20]. As such, NLRP3-driven neuroinflammation presents a potential target for alleviating degenerative neurological disorder development[21]. However, the impact of the NLRP3 inflammasome on BBB integrity remains elusive. While several in vitro studies have suggested that NLRP3 inflammasome activation or the presence of IL-1β may affect tight junction protein expression in endothelial cells[22–24], it is imperative to investigate and validate the potential in vivo impact of the NLRP3 inflammasome on BBB permeability. Understanding the NLRP3-dependent BBB regulation will provide valuable insights into the crucial role of the NLRP3 inflammasome in the neurodegenerative diseases.

As mentioned earlier, the regulation of BBB integrity under various physiological conditions remains unclear. Additionally, despite the growing recognition of the significance of neuroinflammation in the development of neurological diseases, the underlying mechanisms that initiate neuroinflammation remain poorly understood. Here, we present evidence indicating the importance of NLRP3 inflammasome activation in microglia for temporal disruption of the BBB in the context of repetitive mild peripheral inflammation. Notably, our findings also reveal that IL-1β, a major product of inflammasome signaling, does not play a crucial role in peripheral inflammation-induced BBB disruption process.

Results

Peripheral LPS stimulation induces BBB disruption in an NLRP3-dependent manner

To examine whether peripheral inflammation can alter the inflammatory status within the brain, mice were given daily intraperitoneal injection of a mild dose of lipopolysaccharide (LPS, 0.8 mg/kg) according to a previous study with some modification (Fig. 1a)[25]. A single LPS administration (LPS ×1, 6 h post-injection) robustly increased the levels of proinflammatory cytokines such as IL-1β and IL-6 in the circulating blood, but not in the brain (Fig. 1b, c). In contrast, repeated LPS administration with a 24 h-interval (LPS x2) did not stimulate the production of proinflammatory cytokines in the blood, indicating LPS tolerance[26], but caused significant upregulation in IL-1β and IL-6 levels in the brain (Fig. 1b, c; Supplementary Fig. 1a, b).

In this context, we assessed BBB permeability as measured by the extravascular leakage of Evans blue, which was intravenously injected 1 h before euthanization. Similar to cytokine production, repeated LPS stimulation, as opposed to single injection, led to a significant increase in the leakage of Evans blue into the brain (Fig. 1d, e), while intravenous Evans blue freely penetrated other organs regardless of LPS stimulation (Fig. 1d). The LPS-induced increase in BBB permeability persisted for 24 h (Fig. 1f; Supplementary Fig. 1c), but decreased from 48 h post-LPS stimulation (Supplementary Fig. 1d). Additionally, there was no sex-dependent effect on repeated LPS-induced cytokine production and BBB disintegration in the brain. (Supplementary Fig. 1e, f). These findings indicate that repeated peripheral inflammation can induce temporary BBB disruption.

To explore whether peripheral LPS stimulation promotes inflammasome activation within the brain, we used an active caspase-1-specific probe that emits fluorescence only upon the cleavage of active caspase-1[27]. Notably, repeated LPS stimulation, rather than a single administration, led to robust caspase-1 activation in the brain, whereas caspase-1 activation in the spleen or lung was detected even after a single LPS injection (Fig. 1g). Supporting these findings, repeated LPS injection caused IL-1β cleavage within the brain in an NLRP3-dependent manner (Fig. 1h). In addition, *Nlrp3*-deficient mice exhibited reduced production of pro-inflammatory cytokines in the brain in response to peripheral LPS stimulation at the protein (Supplementary Fig. 2a, b) and mRNA (Supplementary Fig. 2c, d) levels.

Along with these cytokine productions, the peripheral inflammation-induced leakage of Evans blue into the brain was significantly decreased in *Nlrp3*-deficient mice (Fig. 1i, j). To further verify this NLRP3-dependent BBB disruption, we performed two-photon intravital imaging to determine the leakage of Texas Red-labeled dextran from blood vessels into the parenchymal region of the brain (Fig. 1k). Repeated LPS stimulation caused a robust increase in dextran fluorescence in the extravascular space (Fig. 1k), which was significantly reduced in *Nlrp3*-deficient mice (Supplementary Fig. 2e; Supplementary Video 1–3). Supporting this finding, we assessed the extravascular leakage of sodium fluoride (NaF) for assaying BBB permeability. Consequently, LPS-induced NaF leakage was also reduced in *Nlrp3*-deficient mice (Fig. 1l). In addition to LPS stimulation, repetitive intravenous injections of a cytokine cocktail containing IL-1β, TNF-α and IL-6 induced BBB permeabilization, which was also NLRP3-dependent (Fig. 1m). These results demonstrate that repeated peripheral inflammation impairs BBB integrity in an NLRP3-dependent manner.

Peripheral LPS stimulation induces circulating immune cell infiltration into the brain and brain-resident glial cell activation in an NLRP3-dependent manner

Given that BBB disruption can lead to subsequent infiltration of circulating immune cells into the brain parenchymal region, we analyzed the population of brain immune cells using flow cytometry (Supplementary Fig. 3a). Repeated LPS stimulation, unlike a single injection, significantly increased $CD45^{+}$ total immune cells and $CD45^{hi}CD11b^{hi}$ brain-infiltrating myeloid cells (Fig. 2a–d), including neutrophils and monocytes (Supplementary Fig. 3b, c). In contrast, the number of brain-resident microglia ($CD45^{int}CD11b^{int}$) was unaffected by single or repeated LPS stimulation (Supplementary Fig. 3d). Consistent with BBB permeability, NLRP3 deficiency significantly reduced the peripheral LPS-induced increase in total brain immune and brain-infiltrating myeloid cells (Fig. 2e–g; Supplementary Fig. 3e). Additionally, two-photon intravital imaging revealed that repeated LPS stimulation promoted the NLRP3-dependent escape of $LysM^{+}$ neutrophils from the vessels into the brain parenchymal regions (Fig. 2h; Supplementary Video 4–6). However, peripheral LPS stimulation did not alter the number of microglia, regardless of NLRP3 presence (Fig. 2i). We then evaluated the effect of the time interval between LPS priming and 2^{nd} LPS stimulation. Notably, unlike the 24 h interval, after 48 h of LPS priming, the 2^{nd} LPS stimulation did not induce significant myeloid cell infiltration into the brain (Fig. 2j, k; Supplementary Fig. 4), indicating that the LPS priming effect might be transient in terms of BBB permeability.

We further assessed the changes in brain-resident glial cells in the hippocampal regions of wild-type (WT) and *Nlrp3*-deficient mice using

https://doi.org/10.1038/s41467-025-56097-1

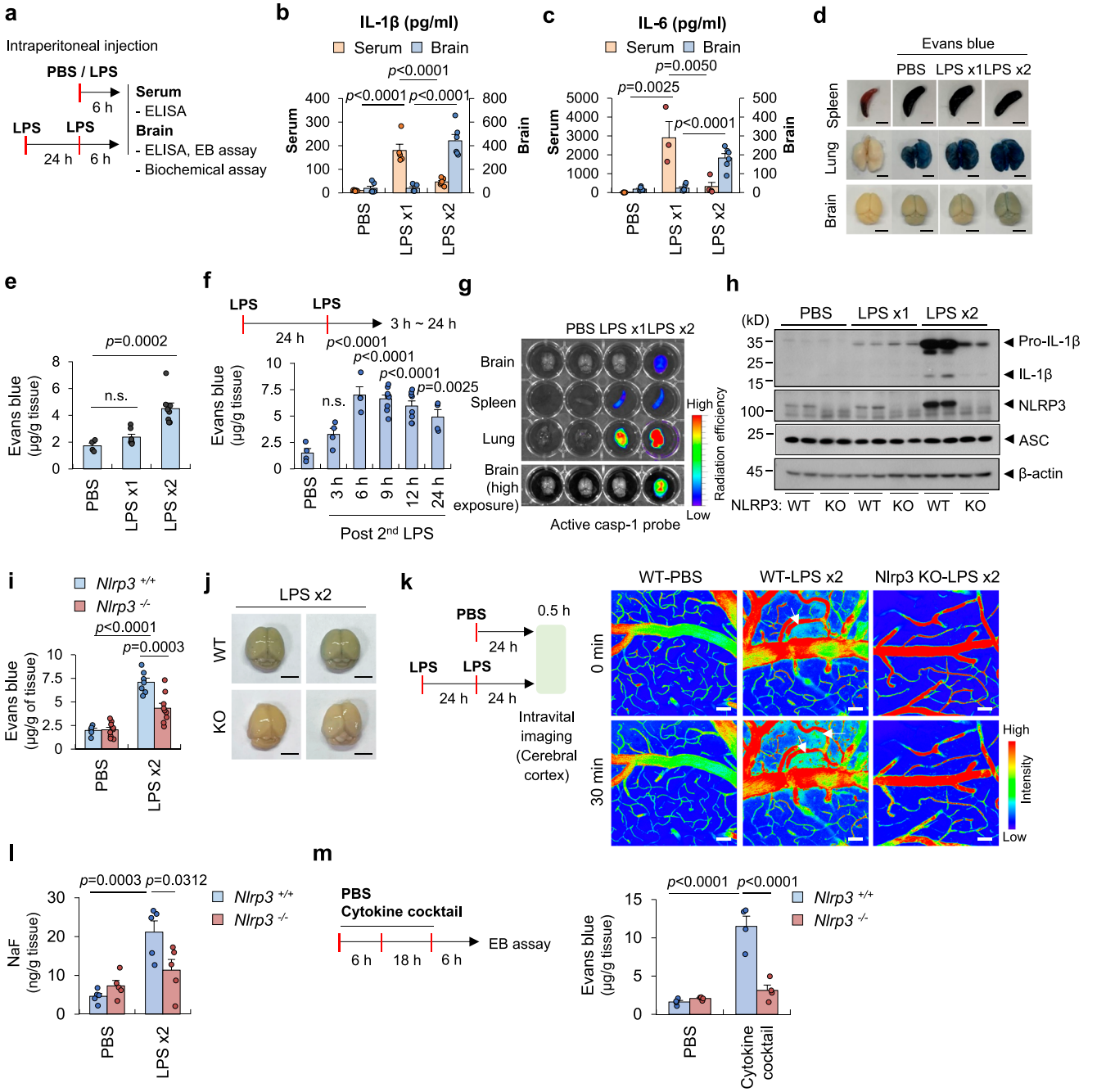

Fig. 1 | Repeated peripheral LPS stimulation induces NLRP3-dependent blood-brain barrier disruption. a Experimental scheme for LPS-induced brain inflammation in mice. **b**, **c** Quantification of IL-1β and IL-6 in the serum and brain extracts of mice administered with PBS or LPS (0.8 mg/kg) at 6 h post last injection. LPS x1, single injection; LPS x2, two consecutive injections with 24 h-interval. (**b** $n = 6$ (PBS, LPSx2), 5 (LPSx1); **c** serum, $n = 4$ (PBS, LPSx2), 3 (LPSx1), brain, $n = 6$ mice per group). **d**, **e** Representative organ images and quantification of Evans blue in the brain of mice injected with PBS or LPS at 6 h post last injection. Scale bars, 0.5 cm. Evans blue was intravenously injected 1 h before sacrifice. ($n = 4$ (PBS), 7 (LPSx1), 8 (LPSx2)). **f** Quantification of Evans blue in the brain tissue at 3–24 h post second LPS injection. ($n = 4$ (PBS, 3, 6, 24 h), 9 (9 h), 8 (12 h)). **g** Ex vivo imaging of active caspase-1 in the various tissues of mice injected with PBS or LPS and caspase-1-activatable probe at 6 h post last LPS injection. **h** Representative immunoblots from brain tissue extracts of wild-type (WT) and NLRP3 knockout (KO) mice injected with PBS or LPS at 6 h post last injection. **i**, **j** Quantification of Evans blue extravasation or representative images in the brain tissue of PBS- or LPS-injected WT ($n = 5$ (PBS), 7 (LPSx2)) and *Nlrp3*$^{-/-}$ ($n = 9$) mice. Scale bars, 0.5 cm. **k** Experimental scheme and representative images of two-photon intravital imaging of cerebral cortex of mice at 24 h post last PBS or LPS injection. Texas Red-dextran (10 kD) was intravenously injected before sacrifice. White arrows indicate the leakage of intravenous dextran. Scale bars, 50 μm. **l** Quantification of NaF extravasation in the brain tissue of WT or *Nlrp3*$^{-/-}$ mice upon PBS or two consecutive LPS injections. ($n = 5$). **m** Quantification of Evans blue in the brain tissue of mice given multiple intravenous injection with PBS or cytokine cocktail (IL-1β 10 μg/kg + IL-6 35 μg/kg + TNFα 35 μg/kg). ($n = 4$) Error bars, s.e.m. One-way ANOVA with Dunnett post hoc test (**b**, **c**, **e**, **f**) and two-way ANOVA with Bonferroni post hoc test (**i**, **l**, **m**). Source data are provided as a Source Data file.

https://doi.org/10.1038/s41467-025-56097-1

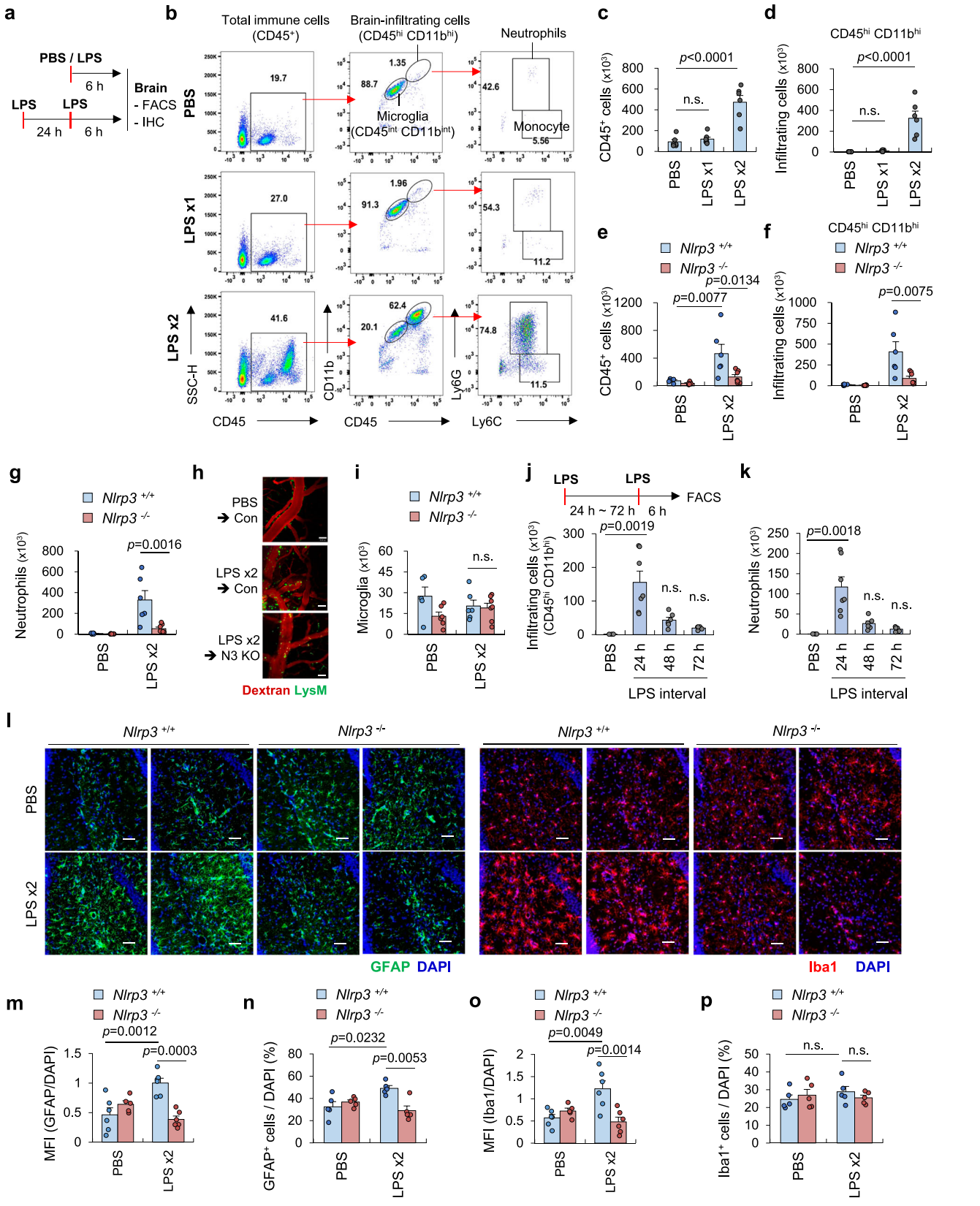

immunofluorescence staining with antibodies targeting astrocyte-specific GFAP and microglia-specific Iba1 (Fig. 2l). Repeated LPS stimulation resulted in a marked increase in the intensity and number of astrocytes in WT mice, which was significantly reduced in the absence of NLRP3 (Fig. 2m, n). In contrast, peripheral LPS stimulation enhanced the intensity of microglia in the WT mouse brain in an NLRP3-dependent manner without affecting the number of microglia (Fig. 2o, p). Repeated LPS stimulation induced significant morphological changes in microglia into their active form, as determined by an increase in soma volume and a decrease in total length (Supplementary Fig. 5a–c), which were significantly reversed by MCC950, a well-known NLRP3-specific inhibitor. These observations indicate that

Fig. 2 | Repeated LPS stimulation induces NLRP3-dependent myeloid cell infiltration into brains and gliosis. a Experimental scheme for flow cytometric analysis or immunohistochemistry of mice brain tissue upon PBS or LPS injection. **b** Representative flow cytometric gating strategy to identify total immune cells, microglia, brain-infiltrating myeloid cells, neutrophils (CD45^{hi}, CD11b^{hi}, Ly6C^{int}, Ly6G^{+}), monocytes (CD45^{hi}, CD11b^{hi}, Ly6C^{+}, Ly6G^{-}) in the brain. **c**, **d** Flow cytometric analysis-based quantification of immune cells and brain-infiltrating myeloid cells in the brain tissue from PBS- or LPS-injected WT mice. ($n = 6$, PBS, LPSx2; 7, LPSx1). **e**–**g**, **i** Quantification of immune cells, brain-infiltrating cells, neutrophils and microglia (**i**) in the brain tissue of PBS- or repeated LPS-injected WT ($n = 5$, PBS; 6, LPSx2) and *Nlrp3*$^{-/-}$ mice ($n = 6$, PBS; 7, LPSx2) by flow cytometric analysis. **h** Representative images of extravascular neutrophils of control (LysM-GFP) and NLRP3 KO (LysM-GFP; *Nlrp3*$^{-/-}$) mice injected with PBS or repeated LPS at 24 h post last LPS injection. Mice were i.v. injected with 70 kDa Texas Red-dextran before sacrifice. Scale bar, 50 μm. **j**, **k** Quantification of brain-infiltrating cells and neutrophils in the brain of PBS- or repeated LPS-administered WT mice by flow cytometry. LPS interval represents the time gap between first and second LPS injection. ($n = 3$, PBS; 7, 24 h; 6, 48 h; 5, 72 h). **l** Representative immunofluorescence images of hippocampal regions of PBS- or repeated LPS-injected WT and *Nlrp3*$^{-/-}$ mice at 6 h post last injection. The brain coronal sections were stained with anti-GFAP (green) and anti-Iba1 (red). DAPI represents nuclei signal (blue). Scale bars, 50 μm. Quantification of the mean fluorescence intensity of GFAP (**m**) and the cell numbers of GFAP^{+} astrocytes (**n**) normalized by DAPI in WT and *Nlrp3*$^{-/-}$ mice upon LPS injections. (**m**, $n = 5$ for KO-PBS, 6 for all other group; **n**, $n = 5$). Quantification of the mean fluorescence intensity of Iba1 (**o**) and the cell numbers of Iba1^{+} microglia (**p**) normalized by DAPI in WT and *Nlrp3*$^{-/-}$ mice upon LPS injections. (**o**, $n = 5$ for KO-PBS, 6 for all other group; **p**, $n = 5$) Error bars, s.e.m. One-way ANOVA with Dunnett post hoc test (**c**, **d**, **j**, **k**) and two-way ANOVA with Bonferroni post hoc test (**e**, **f**, **g**, **i**, **m**, **n**, **o**, **p**). Source data are provided as a Source Data file.

NLRP3 inflammasome is important for the peripheral inflammation-induced activation of brain-resident glial cells.

Peripheral LPS stimulation-induced BBB disruption is IL-1 receptor signaling-independent

Next, we examined whether inhibition of NLRP3 inflammasome signaling could reduce peripheral LPS-induced BBB disruption (Fig. 3a). MCC950, also known as Cytokine release inhibitory drug 3 (CRID3) or CP-456773, was used to block NLRP3 activation (Supplementary Fig. 6a). Intraperitoneal injection of MCC950 resulted in the presence of MCC950 in brain tissues (Supplementary Fig. 6b–d). We also used an IL-1 receptor antagonist (IL-1RA) to inhibit IL-1β signaling (Supplementary Fig. 6e), a major effector molecule of inflammasome response. Notably, MCC950 effectively attenuated repeated LPS-induced Evans blue leakage (Fig. 3b, c). However, IL-1RA failed to inhibit BBB disruption (Fig. 3c). Consistently, IL-1RA did not block peripheral LPS-induced myeloid cell infiltration into the brain, while MCC950 exhibited notable protection that did not reach statistical significance (Fig. 3d–f; Supplementary Fig. 7a, b). These results suggest that IL-1β is not required for the disruption of BBB induced by repeated peripheral inflammation, despite the fact that IL-1β is the main product of NLRP3 inflammasome activation. To further verify the IL-1β-independent BBB disruption, we conducted a BBB permeability assay in IL-1 receptor-deficient mice (Supplementary Fig. 8a). Consistent with the results for IL-1RA, IL-1 receptor deficiency did not affect peripheral LPS-induced Evans blue leakage (Fig. 3g, h) or the recruitment of myeloid cells into the brain (Fig. 3i–k; Supplementary Fig. 8b). To further support these findings, we assessed BBB permeability to observe the leakage of Texas red-labeled dextran (70 kDa) from circulation into the brain parenchymal region (Fig. 3l). Repeated LPS stimulation led to a substantial increase in dextran fluorescence in the hippocampal region of mouse brain, which was significantly reduced in *Nlrp3*-deficient mice (Fig. 3m). However, IL-1 receptor deficiency failed to block peripheral LPS-induced dextran leakage (Fig. 3m). In addition to IL-1β, IL-18 is another inflammasome-specific effector cytokine[28]. However, the level of IL-18 in the brain was low and remained unchanged by peripheral LPS stimulation regardless of NLRP3 presence (Fig. 3n).

To explain the mechanism underlying the NLRP3 inflammasome-dependent BBB impairment beyond IL-1β or IL-18, we examined the role of gasdermin D (GSDMD), which is cleaved by active caspase-1 into an N-GSDMD fragment. The N-GSDMD fragment forms a GSDMD pore on the plasma membrane, which facilitates the secretion of IL-1β and the pyroptosis of inflammasome-active cells[29]. Indeed, *Gsdmd*-deficient bone marrow-derived macrophages failed to secret IL-1β despite intracellular caspase-1 activation (Supplementary Fig. 9a). Notably, GSDMD deficiency significantly attenuated peripheral LPS-induced Evans blue (Fig. 3o; Supplementary Fig. 9b) and NaF (Supplementary Fig. 9c) leakage, suggesting that the GSDMD-mediated release of inflammatory mediators or subsequent pyroptosis is necessary for peripheral inflammation-induced BBB disruption.

Microglial NLRP3-GSDMD activation is important for peripheral inflammation-induced BBB disruption

To gain an insight into the mechanism underlying NLRP3-mediated BBB impairment, we conducted a single cell RNA-sequencing (RNA-seq) analysis on mouse brains, comparing WT and *Nlrp3*-deficient conditions. Control groups were injected with PBS in WT and *Nlrp3*-deficient mice. For the peripheral inflammation group, WT mice were administered with single or repeated LPS injections, while NLRP3 knockout (KO) mice received repeated LPS injections. By performing unsupervised clustering analysis of approximately 110,000 cells that passed quality control, 16 clusters were identified in the Uniform Manifold Approximation and Projection (UMAP) following batch effect correction (Fig. 4a; Supplementary Fig. 10a, b).

Upon repeated LPS stimulation, the population of neutrophils and astrocyte 2 clusters increased substantially (Fig. 4b; Supplementary Fig. 10c) within the brain. Importantly, this increase was NLRP3-dependent (Fig. 4c, d). In contrast, repeated LPS injection reduced the number of endothelial cells, specifically found only in the WT brains (Fig. 4b, c). We then analyzed the expression of inflammasome component proteins on a cluster basis. Notably, brain-resident microglia and brain-infiltrating neutrophils or monocyte-derived macrophages (Mo-Mac) exhibited relatively higher expression of inflammasome components such as NLRP3, Asc (*Pycard*) and caspase-1, along with inflammasome-associated effector molecules such as IL-1β and GSDMD (Fig. 4e, f).

To investigate which specific cell type's NLRP3 inflammasome activity is crucial for peripheral LPS-induced BBB disruption, we generated tamoxifen-inducible cell-specific hyperactive NLRP3 mutant (D301N)-expressing mice (Supplementary Fig. 11a)[30]. This mutant was originally identified in patients with autoinflammatory diseases[31] and is considered a constitutive active form of NLRP3. Using the Cre-Lox system, we first generated mice harboring hyperactive NLRP3 in CX3CR1-expressing cells, such as monocytes and microglia, through tamoxifen injection. Intriguingly, peripheral LPS-induced Evans blue leakage increased significantly in CX3CR1-specific NLRP3 mutant-expressing mice (Fig. 5a; Supplementary Fig. 11b), indicating the importance of NLRP3 in microglia and monocytes. However, astrocyte-specific expression of the NLRP3 hyperactive mutant did not affect peripheral LPS-induced BBB disruption (Fig. 5b; Supplementary Fig. 11c).

To further confirm the role of microglial NLRP3 activation in BBB integrity, we generated mice harboring the NLRP3 mutant in TMEM119-expressing cells, which are more specific to microglia than CX3CR1 (Supplementary Fig. 11d–f). These TMEM119-specific NLRP3 (D301N)-expressing mice exhibited exclusive expression of NLRP3 mutant in microglia upon tamoxifen injection, but not in neutrophils or

https://doi.org/10.1038/s41467-025-56097-1

monocytes (Supplementary Fig. 11g–i). Notably, NLRP3 (D301N) expression in microglia led to a significant increase in the Evans blue leakage by repeated LPS stimulation (Fig. 5c, d). Supporting this observation, the subsequent infiltration of myeloid cells such as neutrophils into the brain was significantly increased in microglia-specific NLRP3 mutant-expressing mice in response to repeated LPS injections (Fig. 5e, f; Supplementary Fig. 12a). In contrast, LPS-driven infiltration of neutrophils into the lungs was not affected in TMEM119-specific hyperactive NLRP3-expressing mice (Supplementary Fig. 12b, c). These findings indicate that TMEM119-dependent microglial expression of NLRP3 (D301N) enhances peripheral inflammation-induced neutrophil infiltration into the brain, but not into peripheral organs such as the lungs.

To examine the potential role of microglial GSDMD-mediated pyroptosis in NLRP3-dependent BBB impairment, we generated microglia-specific (*Tmem119-creER*) *Gsdmd*-deficient mice (Supplementary Fig. 13a). Notably, tamoxifen-induced GSDMD depletion in microglia significantly reduced peripheral LPS-induced Evans blue leakage (Fig. 5g; Supplementary Fig. 13b) and neutrophil infiltration into the brain (Fig. 5h; Supplementary Fig. 14a). However, these microglial *Gsdmd*-deficient mice exhibited comparable levels of myeloid cell infiltration ($CD45^{hi}CD11b^{hi}$) and showed increased neutrophil

https://doi.org/10.1038/s41467-025-56097-1

Fig. 3 | IL-1R signaling is not required for peripheral inflammation-induced BBB disruption and myeloid cell infiltration into brains. a Experimental scheme for pretreatment of MCC950 or IL-1RA (10 mg/kg) 30 min before PBS or LPS injection. **b**, **c** Representative images or quantification of Evans blue extravasation into the brain in response to the repeated LPS injection into mice pretreated with MCC950 or IL-1RA. Scale bars, 0.5 cm. ($n = 9$, PBS, LPSx2; 6, MCC, IL-1RA group). **d** Representative flow cytometric analysis depicting the population of immune cells ($CD45^+$) in the mouse brains stimulated as in **b** and **c**. **e**, **f** Flow cytometric analysis-based quantification of brain-infiltrating myeloid cells and neutrophils in the brain of PBS- or LPS-treated mice with MCC950 and IL-1RA pretreatment. ($n = 7$ for MCC group; 5 for all other group). **g**, **h** Quantification and representative images of Evans blue extravasations in WT and *Il1r1*$^{-/-}$ mice brain upon LPS injections. Scale bars, 0.5 cm. ($n = 5$, PBS, 9, LPSx2, WT; $n = 6$, PBS, 8, LPSx2, *Il1r1*$^{-/-}$). **i** Representative flow cytometric analysis of brain illustrating the population of immune cells ($CD45^+$) in the WT and *Il1r1*$^{-/-}$ mice upon repeated LPS injections. **j**, **k** Flow cytometric analysis-based assessment of brain-infiltrating cells and neutrophils in the WT and *Il1r1*$^{-/-}$ mice brain upon repeated LPS injections. ($n = 5$). **l** Representative immuno-fluorescence images of brain hippocampal region from WT, *Nlrp3*$^{-/-}$, and *Il1r1*$^{-/-}$ mice upon repeated LPS stimulation, followed by Texas red-dextran injection 1 h before sacrifice. DAPI represents nuclei signal (blue). Scale bars, 100 μm. **m** Quantification of dextran fluorescence normalized by DAPI in the hippocampal region of WT ($n = 11$), *Nlrp3*$^{-/-}$ ($n = 7$), and *Il1r1*$^{-/-}$ ($n = 8$) mice treated as in **l**. **n** Quantification of IL-18 in the brain extracts of WT ($n = 4$, PBS; 5, LPSx2) and *Nlrp3*$^{-/-}$ mice ($n = 5$, PBS; 6, LPSx2) upon repeated LPS injections. **o** Quantification of Evans blue deposition in the brain of WT ($n = 3$, PBS; 6, LPS x2) and *Gsdmd*$^{-/-}$ mice ($n = 7$, PBS; 12, LPS x2) upon repeated LPS injections. Error bars, s.e.m. One-way ANOVA with Dunnett post hoc test (**c**, **e**, **f**, **m**) and two-way ANOVA with Bonferroni post hoc test (**g**, **j**, **k**, **n**, **o**). Source data are provided as a Source Data file.

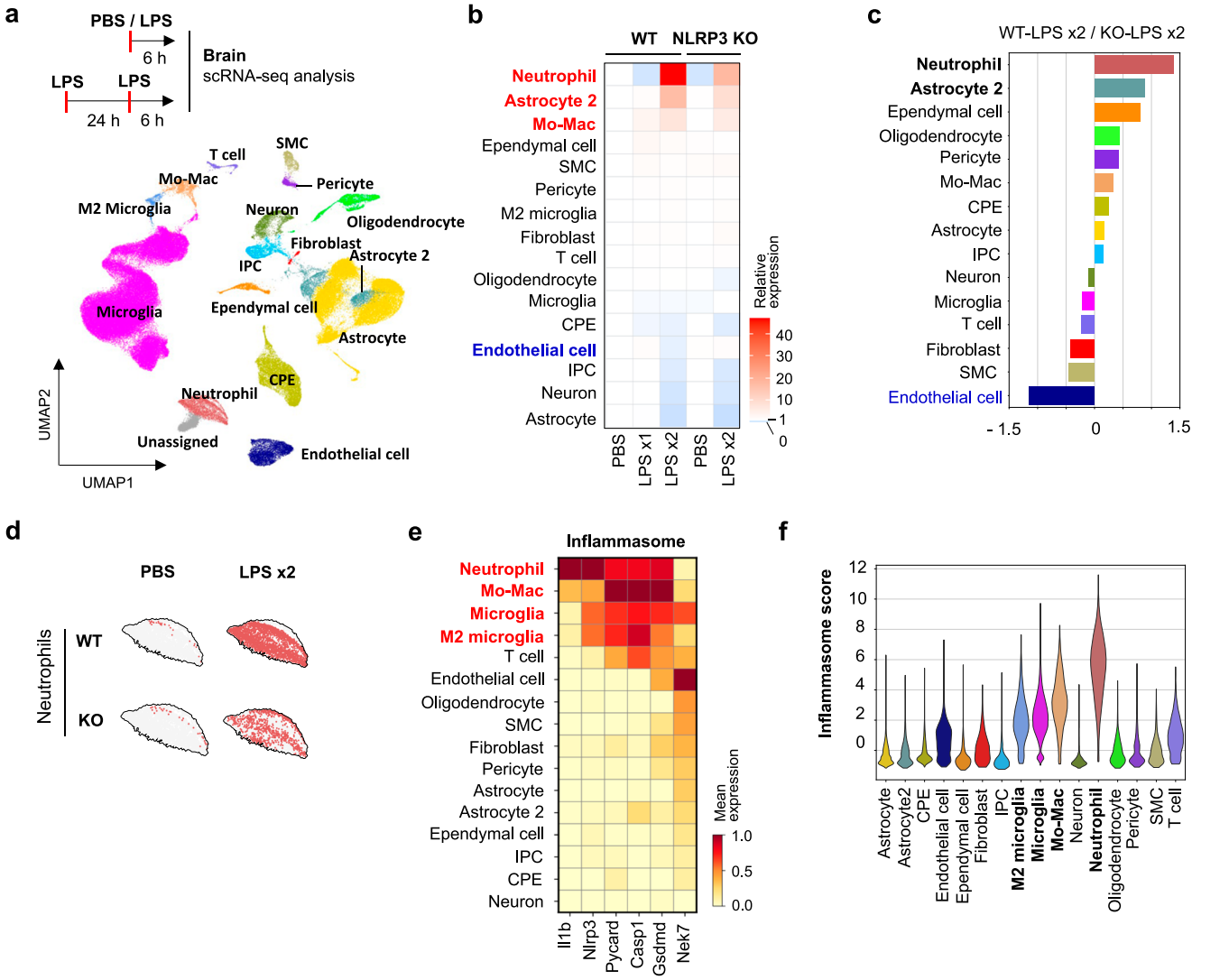

Fig. 4 | Single-cell RNA sequencing analysis of mouse brains following repeated LPS stimulation. a UMAP plots of single-cell RNA sequencing data encompassing 105,838 genes, displaying a comprehensive single-cell map of the mouse brain. The merged dataset incorporates samples from PBS- or LPS-injected WT and NLRP3 KO groups. The UMAP visualization delineates the intricate cellular landscape into 17 distinct and color-coded clusters. **b** Representation of cell cluster ratios in each group relative to the WT-PBS group. Color intensity reflects the difference in ratio between the WT-PBS group and each respective group. **c** Bar plot depicting the log2 fold changes (log2FC) of each cell type when comparing the WT-LPS x2 group versus the KO-LPS x2 group. Bars on the right side indicates an increase in the WT-LPS x2 group, while those on the left side signify an increase in the KO-LPS x2 group. **d** UMAP plots of neutrophil clusters of PBS- or LPS-injected WT and NLRP3 KO mice. **e** Heatmap illustrating the expression of inflammasome marker genes in each cluster. Color intensity indicates scaled mean expression level. **f** VISION scoring of inflammasome genes on all cell clusters within all samples. The violin plot illustrates the inflammasome score using genes derived from **e**.

https://doi.org/10.1038/s41467-025-56097-1

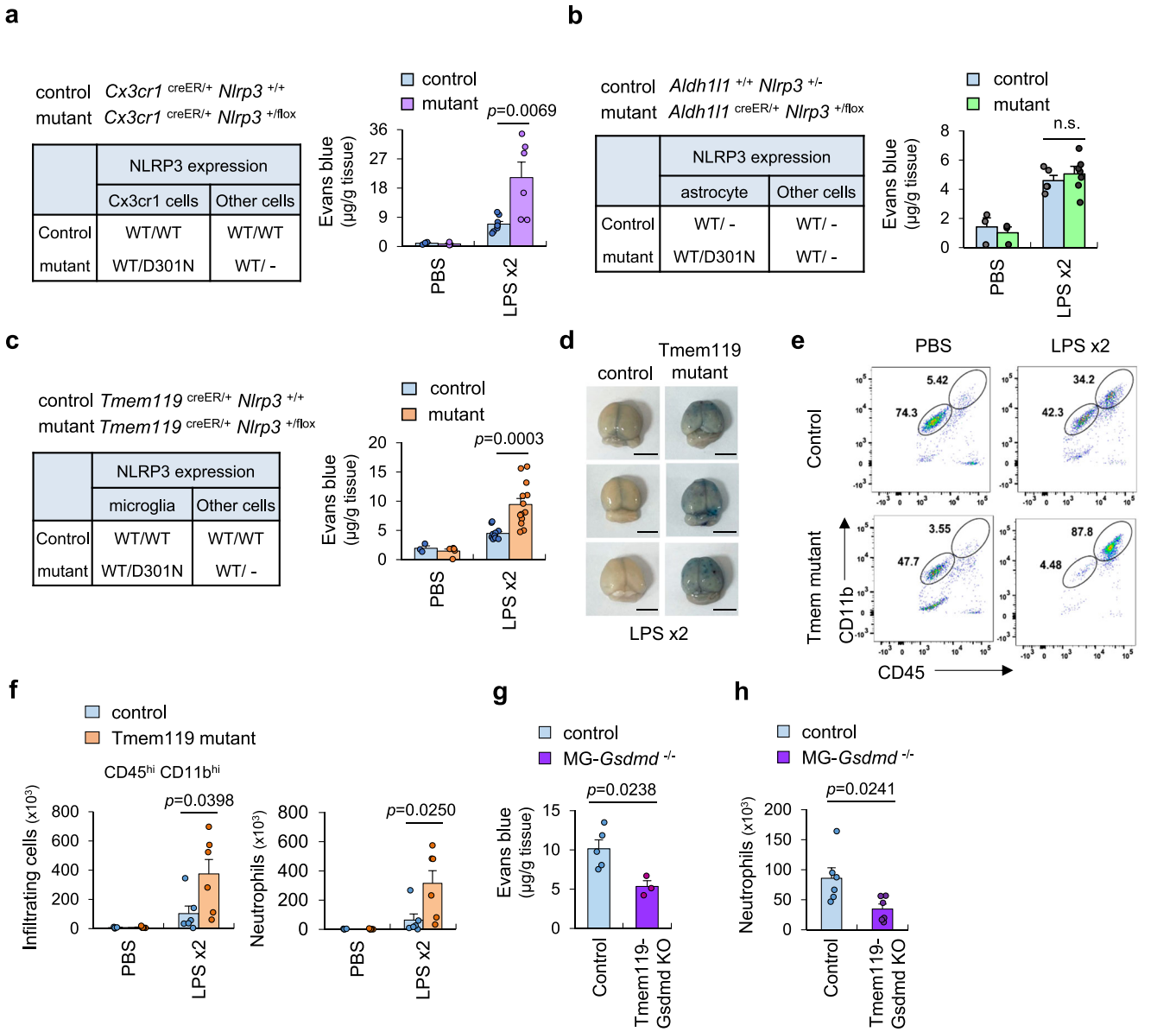

Fig. 5 | Contribution of microglial NLRP3 inflammasome activation to peripheral LPS-induced BBB disruption. Summary of NLRP3 expression in Cx3cr1^{+} (**a**) or Aldh1l1^{+} cells (**b**) and other cell types of control and NLRP3 mutant (D301N)-expressing mice upon tamoxifen treatment (left panel). Quantification of Evans blue extravasation in the tamoxifen-treated control (**a**, $n = 3$, PBS, 8, LPS x2; **b**, $n = 3$, PBS, 5, LPS x2) and NLRP3 mutant (**a**, $n = 3$, PBS, 6, LPS x2; **b**, $n = 3$, PBS, 7, LPS x2) mice brain upon PBS or repeated LPS injection (right panel). **c** Summary of NLRP3 expressions in Tmem119^{+} cells and other cell types of control and NLRP3 mutant mice upon tamoxifen treatment (left panel). Quantification of Evans blue extravasation (right panel) in the tamoxifen-treated control and mutant mice brain upon PBS or repeated LPS injection. ($n = 3$, PBS, 11, LPS x2, control; $n = 5$, PBS, 13, LPS x2, mutant). **d** Representative images of brain as in **c**. **e** Representative flow cytometric analysis of brain illustrating the population of microglia and brain-infiltrating myeloid cells (CD45^{hi} CD11b^{hi}) in the control and NLRP3 mutant (Tmem119^{creER}) mice upon PBS or repeated LPS injections. Scale bars, 0.5 cm. **f** Quantification of brain-infiltrating myeloid cells or neutrophils in **e**. ($n = 4$, PBS, 6, LPS x2, control; $n = 6$, mutant). **g** Quantification of Evans blue depositions in the tamoxifen-treated control mice (*Gsdmd*$^{flox/flox}$, $n = 5$) and microglia (MG)-specific *Gsdmd*$^{-/-}$ mice (*Tmem119*$^{creER/+}$; *Gsdmd*$^{flox/flox}$, $n = 3$) upon repeated LPS injection. **h** Quantification of neutrophils in the brain of control and MG-*Gsdmd*$^{-/-}$ mice upon repeated LPS injection by flow cytometry. ($n = 6$) Error bars, s.e.m. Unpaired two-sided Student's *t* test (**g**, **h**) and two-way ANOVA with Bonferroni post hoc test (**a**–**c**, **f**). Source data are provided as a Source Data file.

infiltration into the lungs following peripheral LPS injection, compared to control mice (Supplementary Fig. 14b, c). These results demonstrate that repeated peripheral inflammation promotes BBB disruption via activation of NLRP3-GSDMD signaling in microglia.

Peripheral inflammation induces NLRP3-dependent reprogramming in BBB-composing cells towards chemotaxis and immune cell migration

To investigate inflammasome-driven alterations in BBB-comprising cells, we performed differentially expressed genes (DEGs) analysis in endothelial cells from WT and *Nlrp3*-deficient mouse brains. Upon comparing the WT-PBS group with the WT-LPS x2 group, we observed a significant increase in the expression of 1,644 genes by more than two-fold in the LPS-stimulated group (Fig. 6a). Subsequently, we compared the WT-LPS x2 and NLRP3 KO-LPS x2 groups, uncovering 314 genes exhibiting increased expression in the WT-LPS x2 group by more than 1.4 times (Fig. 6a). Remarkably, 33 genes were found to overlap between the two gene lists, displaying distinct and significant expression in the WT-LPS x2 groups (Fig. 6b). This overlapped gene lists from two comparisons are termed in NLRP3-LPS x2-specific or

https://doi.org/10.1038/s41467-025-56097-1

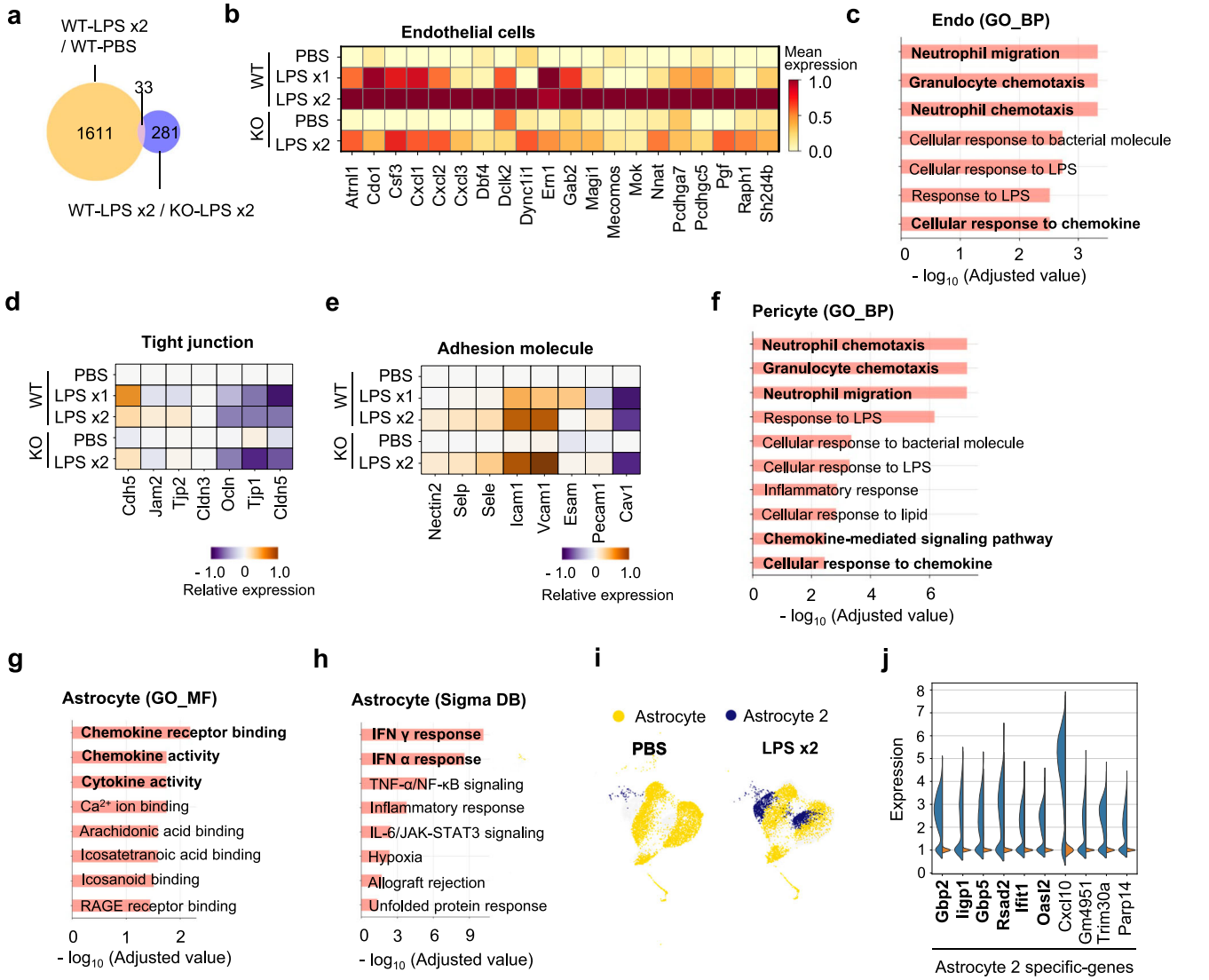

Fig. 6 | NLRP3 inflammasome leads to the reprogramming of BBB-composing cells toward chemotaxis and cell migration. a Venn diagram illustrating the number of genes specifically upregulated in brain endothelial cells following LPS x2-treated versus PBS-treated group in WT mice (orange, fold change >2, $p < 0.05$) and genes upregulated in WT-LPS x2 versus KO-LPS x2 (blue, fold change >1.4, $p < 0.05$). **b** Heatmap presenting 20 genes notably upregulated in the WT LPS x2 group from **a** excluding unannotated genes. Color intensity indicates scaled mean expression level. **c** Gene Ontology (GO) analysis results for 33 genes identified in **a**, depicting enriched terms in GO Biological Processes (BP). Heatmap illustrating the expression of major tight junction genes (**d**) or adhesion molecules (**e**) in the brain endothelial cells of WT and *Nlrp3*-deficient mice following PBS or LPS stimulations. Barplots illustrating WT LPS x2-specific terms identified in gene ontology: **f** pericyte in GO BP, **g** astrocytes in GO Molecular Function (MF), and **h** astrocytes in Sigma DB. These analysis utilized genes particularly increased in the WT LPS x2 group compared to both the WT PBS and KO LPS x2 group. **i** UMAP plot displaying astrocyte and astrocyte2 clusters in WT-PBS and WT-LPS x2 group. **j** Violin plot showing the expression of top 10-upregulated genes in astrocyte 2 compared to astrocyte cluster. Bold denotes IFN-related or stimulated genes.

NLRP3-specific DEGs. Gene ontology (GO) analysis of NLRP3-specific upregulated genes in endothelial cells revealed their association with myeloid cell migration and chemotaxis (Fig. 6c). Additionally, we examined changes in the expression of major tight junction proteins and adhesion molecules in endothelial cells. Transcriptomic analysis showed that repeated LPS stimulation led to the upregulation and downregulation of tight junction proteins (Fig. 6d), but no significant differences between WT and *Nlrp3*-deficient mice were observed. Moreover, peripheral LPS stimulation caused upregulation of most adhesion molecules in the endothelial cells; however, this upregulation was independent of NLRP3 presence (Fig. 6e).

Similarly, we examined NLRP3-LPSx2-specific DEGs in pericytes and identified 69 overlapping genes from two comparisons (Supplementary Fig. 15a, b). GO analysis of NLRP3-LPSx2-specific DEGs in pericytes also showed a strong association with chemotaxis and migration of granulocytes such as neutrophils (Fig. 6f). In accordance with these observations, GO analysis of 148 NLRP3-LPSx2-specific genes in astrocytes (Supplementary Fig. 15c) indicated significant changes related to the chemotaxis and cell migration (Fig. 6g; Supplementary Fig. 15d, e). Intriguingly, NLRP3-specific DEGs in astrocytes exhibited noticeable alterations in chemokine signaling and interferon (IFN) response (Fig. 6g, h). Besides, repeated LPS stimulation induced the expansion of astrocyte 2 subsets. (Fig. 6i; Supplementary Fig. 16a). Many genes with increased expression specific to this astrocyte 2 cluster were related to type 1 IFN response (Fig. 6j; Supplementary Fig. 16b). However, the expression levels of astrocyte endfoot genes, critical for BBB integrity, were not significantly affected by the NLRP3 inflammasome in the astrocyte 2 cluster (Supplementary Fig. 16c). We also explored potential NLRP3-dependent changes in astrocyte-microglia communications, as microglia were the primary

inflammasome-active cells. Using NicheNet analysis under repeated LPS-stimulated conditions, we observed 750 WT-specific interactions between astrocytes (including astrocyte 2) and microglia, considering astrocyte and astrocyte 2 as sender cells and microglia as receivers, compared to only 109 interactions in the NLRP3 KO condition (Supplementary Fig. 16d, e). Similarly, WT-specific signaling from astrocytes and microglia to astrocyte 2 reached 925 interactions, versus 108 in the NLRP3 KO mice. These results suggest that NLRP3 signaling enhances astrocyte-microglia communication, which may play a role in NLRP3-mediated BBB permeability.

Given that microglial heterogeneity has been implicated in the neurodegenerative diseases, we conducted sub-clustering of microglia and annotated them into 6 subclusters (Fig. 7a). Notably, interferon-stimulated genes (ISGs) cluster exhibited specific increases in the LPS x2 groups of WT mice (Supplementary Fig. 17a) and DEG analysis revealed them to be mainly associated with IFN responses (Fig. 7b). To further elucidate the differences between WT and NLRP3 KO in microglia, we performed a trajectory analysis (Fig. 7c; Supplementary Fig. 17b). The analysis identified a 'homeostatic' cluster as the starting point and a 'phagocytotic' cluster as the ending point in all groups (Fig. 7c, lower left). However, LPS x2 stimulation caused two additional endpoints: an ISGs cluster (Fig. 7c, lower middle) and DAM1 (damage-associated microglia1) cluster (Fig. 7c, lower right). Density analysis using UMAP revealed a clear difference between WT and NLRP3 KO at the LPS x2 level (Fig. 7d). In the WT-LPS x2 group, microglia reached both ISG-high and DAM1 endpoints, while in the KO-LPS x2 group, the trajectory halted midway (Fig. 7d). These results suggest that NLRP3 inflammasome activity drives microglia reprogramming toward ISG and DAM1 phenotypes.

Next, we analyzed NLRP3-LPSx2-specific DEGs in the whole clusters (Supplementary Data 1) and identified 30 genes that were specifically upregulated in the WT-LPS x2 group (Fig. 7e; Supplementary Fig. 18a). Most of the NLRP3-dependent upregulated genes in all clusters were IFN-related genes or ISGs (Fig. 7f, bold). GO analysis of NLRP3-specific genes also revealed a significant increase in type 1 IFN-related genes (Supplementary Fig. 18b–d). We thus examined the expression of IFN-β in brain extracts and observed NLRP3-specific upregulation of *Ifnb1* mRNA in the mouse brain 3 h after the 2nd LPS stimulation (Supplementary Fig. 19a). Among the NLRP3-specific ISGs, the expression of the *Rsad2* gene, encoding viperin, was upregulated in the brains of WT mice (Supplementary Fig. 19b, c). However, *Rsad2*-deficiency did not significantly attenuate the peripheral LPS-induced myeloid cell infiltration into the brain (Fig. 7g, h; Supplementary Fig. 20a). Additionally, interferon-α receptor 1 (*Ifnar1*)-deficient mice exhibited no difference in BBB permeability at 6 h after 2nd LPS injection (Fig. 7i; Supplementary Fig. 20b, c). However, LPS-induced myeloid cell infiltration was significantly reduced in *Ifnar1*-deficient mice at 12 h post 2nd LPS injection (Fig. 7j; Supplementary Fig. 20d). These results suggest that type 1 IFN signaling might be implicated downstream of the NLRP3 inflammasome, contributing to BBB disruption; however, the detailed molecular targets remain to be resolved.

Microglial NLRP3-GSDMD axis facilitates neutrophil-specific chemokines production in BBB-composing cells

NLRP3-specific DEG and GO analysis revealed that inflammasome activation significantly altered the expression of genes related to chemotaxis or chemokine signaling in the BBB. In this context, we analyzed the chemokine transcriptome levels of all clusters in response to LPS stimulation (Supplementary Fig. 21a). Several chemokines such as *Cxcl5*, *Ccl20*, and *Cxcl3* mRNA were upregulated by peripheral LPS stimulation only in NLRP3-expressing WT mice (Fig. 8a). We also examined chemokine levels in BBB-comprising cells and microglia (Supplementary Fig. 21b), and in endothelial cells (Fig. 8b; Supplementary Fig. 21c), and noticed that some chemokines (*Cxcl1*, *Cxcl2*, *Cxcl3*, *Cxcl5* and *Cxcl10*) were commonly upregulated in an NLRP3-dependent manner. In accordance with these transcriptomic analyses, repeated LPS stimulation induced CXCL1 and CXCL2 production in whole mouse brain extracts (Supplementary Fig. 21d, e). Intriguingly, the production of these chemokines was significantly decreased by NLRP3 or GSDMD deficiencies, but not by the deficiency of the IL-1 receptor (Fig. 8c, d; Supplementary Fig. 21f, g). Consistent with these observations, microglia-specific hyperactive NLRP3 mutant-expressing mouse brains exhibited increased *Cxcl1* mRNA expression after repeated LPS stimulation (Fig. 8e). In contrast, microglia-specific deletion of GSDMD significantly reduced repeated LPS-induced *Cxcl1* and *Cxcl2* mRNA production in the brain (Fig. 8f). These results collectively indicate that the microglial NLRP3-GSDMD signaling is important for peripheral inflammation-induced production of these CXCL chemokines in the brain.

To gain an insight into how NLRP3-GSDMD activation in microglia triggers CXCL chemokine production, we performed mass spectrometry-based bottom-up proteomics of culture supernatants from WT and *Gsdmd*-deficient microglia (Fig. 8g). We first selected candidates that showed more than a 1.3-fold increase in the LPS + ATP-treated group compared to the PBS-treated group. Next, we excluded inflammasome-independent secreted proteins that exhibited more than a 1.3-fold increase in ATP-treated group relative to the PBS group. We then compared the WT-LPS + ATP group to the GSDMD KO-LPS + ATP group and sorted the proteins based on this criterion. This analysis identified top 11 NLRP3-GSDMD-specific secreted proteins (Fig. 8h). Among these, growth differentiation factor-15 (GDF-15) was further validated through targeted mass spectrometry (Supplementary Fig. 22a). Intriguingly, repeated LPS injection led to a significant increase in GDF-15 levels in brain tissue homogenates from wild-type mice, but not in those from *Nlrp3*- or *Gsdmd*-deficient mice (Fig. 8i, j; Supplementary Fig. 22b). Transcriptomic analysis further confirmed considerable expression of *Gdf-15* in microglia (Supplementary Fig. 22c). To assess whether GDF-15 influences CXCL chemokine production, we treated mixed glial cultures with recombinant GDF-15. This treatment led to a robust increase in *Cxcl1*, *Cxcl2* and *Cxcl3* mRNA levels (Fig. 8k) Supporting this finding, intravenous GDF-15 injections significantly elevated CXCL1 and CXCL2 protein levels (Fig. 8l, m) and mRNA expression (Supplementary Fig. 22d, e). Additionally, in mixed glial cells, GDF-15 induced CXCL1 production in an NF-κB- or MEK-dependent manner (Supplementary Fig 22f). These findings suggest that NLRP3-GSDMD activation promotes CXCL chemokine production at the BBB by inducing GDF-15 secretion.

Neutrophil recruitment contributes to peripheral inflammation-induced BBB disruption

Of notice, CXCL chemokine production was higher 3 h after 2nd LPS stimulation than at 6 h (Fig. 8c, d). Additionally, time-dependent experiments revealed that brain inflammasome activation was observed from 3 h after the 2nd LPS treatment (Fig. 9a). Instead, myeloid cell infiltration was markedly increased 5 h after 2nd LPS stimulation (Fig. 9b, c; Supplementary Fig. 23). These findings suggest that inflammasome-dependent chemokine production may trigger the recruitment of circulating neutrophils. We then examined the mRNA expression of chemokine receptors in brain-infiltrated neutrophils and found higher expression of *Cxcr2* and *Ccr1* (Fig. 9d). CXCR2 is specific to NLRP3-dependent upregulated chemokines, such as CXCL1, CXCL2, CXCL3 and CXCL5[32].

Cell-cell communication analysis in CXCL signaling using CellChat revealed that a prevalent activation of the CXCL signaling pathway in the WT-LPS x2 groups was evident compared to that in other groups (Fig. 9e). In particular, CXCL1- and CXCL2-CXCR2 signaling-related pathways were prominent in the WT-LPS x2 group, but much less in the *Nlrp3*-deficient cells. These pathways influence the interactions of neutrophils with endothelial cells, microglia, or pericyte in the WT-LPS x2 group. These findings suggest that the interactions mediated by the

https://doi.org/10.1038/s41467-025-56097-1

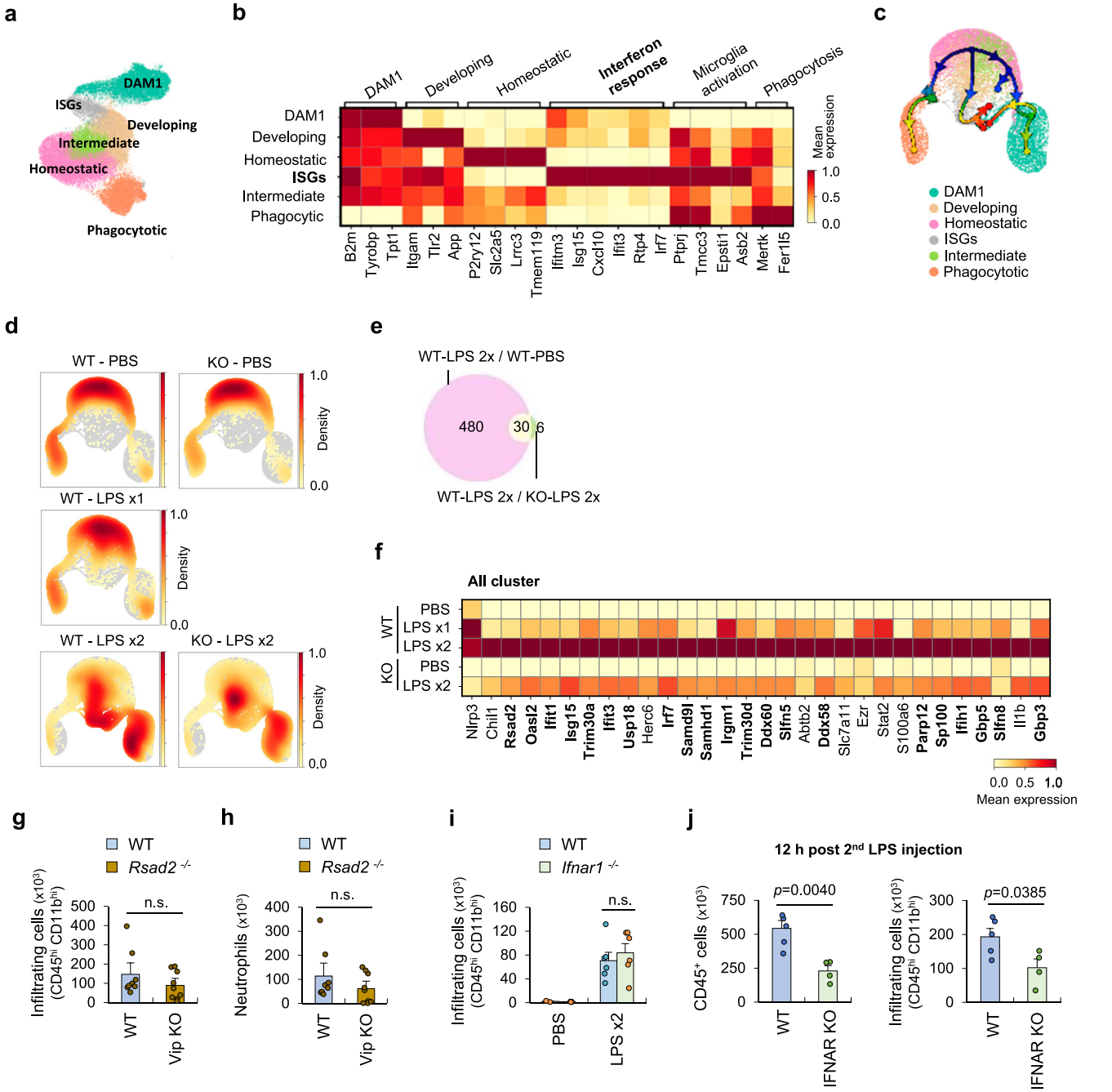

Fig. 7 | NLRP3 inflammasome-dependent upregulation of type 1 interferon-related genes in microglia and all brain cell clusters. a UMAP plot displaying 6 subclusters of microglia. **b** Heatmap illustrating categories presenting specific functional terms in microglia subclusters. **c** Trajectory analysis illustrating the microglial fate directions between distanced cluster lineages. UMAP visualization is color-coded to represent subclusters of microglia or outlining the trajectory from homeostatic microglia to distinct subtypes in ISGs and DAM1. **d** UMAP visualization depicting the density of microglia cells for each experimental group with density values scaled between 0 and 1. **e** Venn diagram showing the number of genes specifically increased in all clusters in WT LPS x2 group versus WT PBS group (fold change >1.5, $p < 0.05$) and versus KO LPS x2 group (fold change >1.5, $p < 0.05$). **f** Heatmap displaying NLRP3-specific increased 30 genes derived from **e**, with unannotated genes excluded. **g**, **h** Quantification of brain-infiltrating myeloid cells or neutrophils in the brain of repeated LPS-treated WT and *Rsad2*-deficient mice at 6 h post last injection. ($n = 8$, WT; $n = 9$, *Rsad2*-deficient mice). **i**, **j** Quantification of brain-infiltrating myeloid cells or total brain immune cells ($CD45^+$) in the brain of PBS^- or repeated LPS-treated WT and *Ifnar1*-deficient mice at 6 h (**i**) or 12 h (**j**) post last injection. (**i**, $n = 3$, PBS, 6, LPS x2; **j**, $n = 5$, PBS, 4, LPS x2). Color intensity indicates scaled mean expression level (**b**, **f**). Error bars, s.e.m. Unpaired two-sided Student's *t* test (**g**, **h**, **j**) and two-way ANOVA with Bonferroni post hoc test (**i**). Source data are provided as a Source Data file.

CXCL signaling between neutrophils and BBB cells are NLRP3-dependent, unveiling the intricate role of NLRP3 inflammasome in modulating neutrophil recruitment and BBB integrity during inflammation.

Then, to examine whether the recruited neutrophils can contribute to BBB disruption, we depleted neutrophils using anti-Ly6G antibodies prior to LPS stimulation (Supplementary Fig. 24). Notably, neutrophil ablation significantly reduced peripheral inflammation-induced BBB disruption (Fig. 9f; Supplementary Fig. 25a). Accordingly, neutrophil recruitment blockade by the CXCR2 antagonist SB225002 also significantly attenuated LPS-promoted BBB permeabilization

https://doi.org/10.1038/s41467-025-56097-1

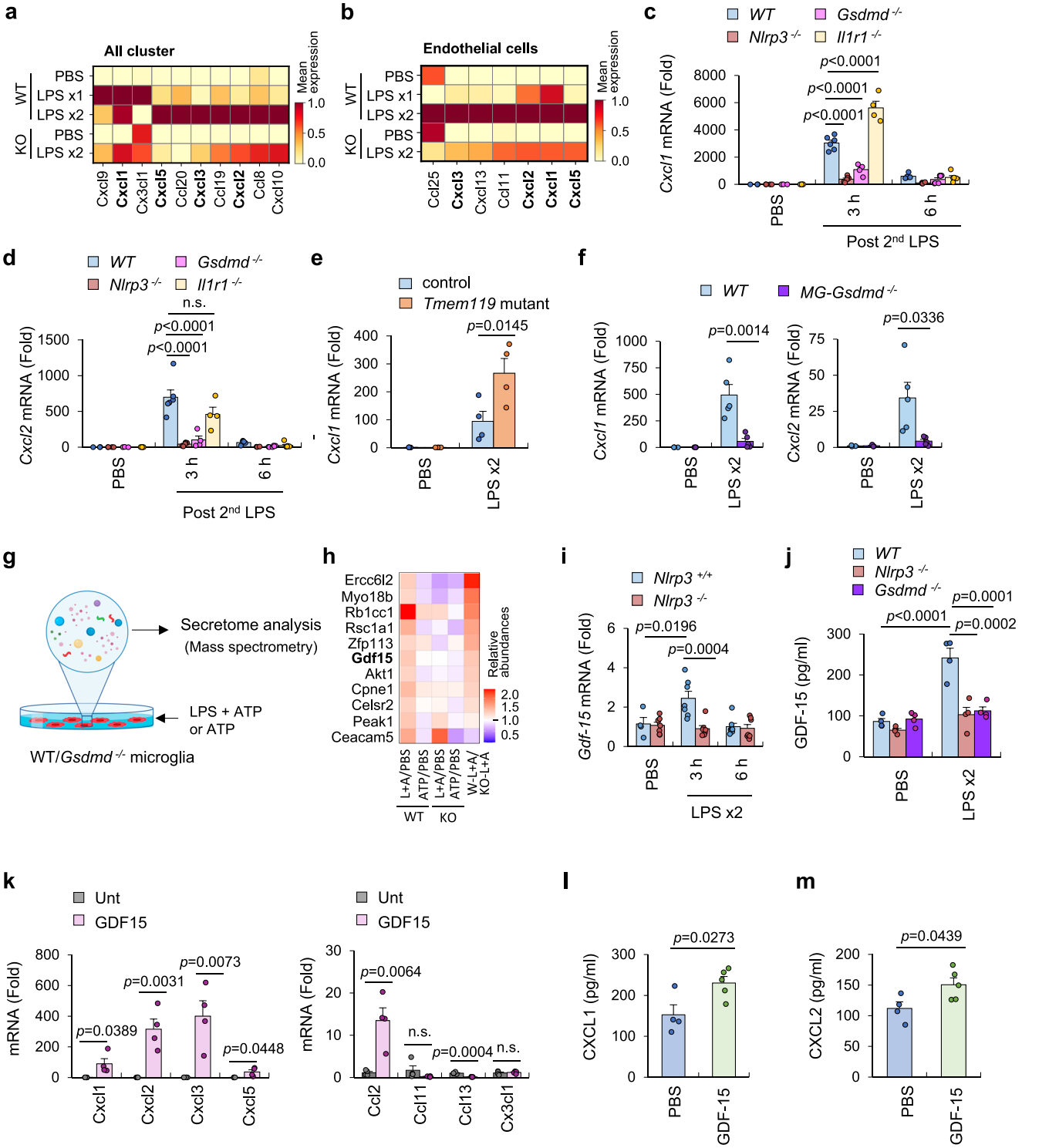

(Fig. 9g; Supplementary Fig. 25b). In contrast, deficiency of CCR2, essential for monocyte recruitment, did not affect BBB integrity in response to repeated LPS stimulation (Fig. 9h; Supplementary Fig. 25c). These findings indicate that inflammasome-dependent neutrophil recruitment into the blood vessels in the brain contributes to BBB breakdown.

To investigate how resident microglia and recruited neutrophils facilitate BBB breakdown, we examined expression of matrix metalloproteinases (MMPs), which are crucial for BBB disruption[33,34], in brain extracts. Notably, scRNA-seq analysis revealed that repeated LPS stimulation increased the expression of some MMPs, such as MMP8 and 9, in an NLRP3-dependent manner (Fig. 10a; Supplementary Fig. 26a). These NLRP3-dependent MMPs were highly expressed in neutrophils (Fig. 10b; Supplementary Fig. 26b). Indeed, repeated LPS injection led to a significant production of MMP9 protein in the brain tissue (Supplementary Fig. 26c). As MMP production in the brain increased from 4 h after 2nd LPS stimulation (Fig. 10c), cells other than neutrophils might also produce MMPs in response to NLRP3 activation. Consistent with the scRNA-seq data, MMP8 or MMP9 production was impaired in the brain extracts of *Nlrp3*-deficient mice and of microglia-specific *Gsdmd*-deficient mice (Fig. 10d–g) but not of *Il1r*-dericient mice upon repeated LPS stimulation (Supplementary Fig. 26d).

Fig. 8 | Microglial NLRP3-GSDMD activation induces the production of Cxcr2-specific chemokines via releasing GDF-15. a, **b** Heatmap illustrating the NLRP3-dependent increased expression of chemokine genes across all groups in all clusters or endothelial cells. Color intensity indicates scaled mean expression level. **c**, **d** Quantification of mRNA levels of *Cxcl1* and *Cxcl2* in the whole brain extracts of PBS- or repeated LPS-injected WT, *Nlrp3*$^{-/-}$, *Gsdmd*$^{-/-}$, and *Il1r1*$^{-/-}$ mice at 3 h or 6 h after the last injection. (The number of biological replicates was presented in the order of PBS, 3 h, 6 h; $n = 3, 6, 5$, WT; 4, 6, 4, *Nlrp3*$^{-/-}$; 3, 4, 6, *Gsdmd*$^{-/-}$; 4, 4, 6, *Il1r1*$^{-/-}$ mice). **e** Quantification of brain mRNA level of *Cxcl1* in control and Tmem119-specific NLRP3 mutant (D301N)-expressing mice at 6 h post second LPS injection. ($n = 4$). **f** Quantification of brain mRNA levels of *Cxcl1* and *Cxcl2* in control (*Gsdmd*$^{flox/flox}$) and MG-*Gsdmd*$^{-/-}$ mice (*Tmem119*$^{creER/+}$; *Gsdmd*$^{flox/flox}$) upon PBS ($n = 3$) or repeated LPS ($n = 5$) injection by flow cytometry. **g** Experimental scheme to isolate secretome from microglia treated with LPS (0.25 μg/ml, 3 h) followed by ATP treatment (2.5 mM, 20 min). **h** Heatmap illustrating the relative concentration of target proteins in the culture supernatant from WT or *Gsdmd*$^{-/-}$ (KO) microglia upon appropriate treatments as determined by mass spectrometric analysis. L + A denotes LPS + ATP treatment as in **g**. Color intensity indicates relative abundances of targeted proteins. **i** Quantification of *Gdf15* mRNA levels in the brain tissues of PBS- or repeated LPS-treated WT and *Nlrp3*$^{-/-}$ mice. ($n = 4$, WT-PBS; 7, all other group). **j** Quantification of GDF15 protein levels in the brain tissues of PBS- or repeated LPS-treated WT and *Nlrp3*$^{-/-}$, *Gsdmd*$^{-/-}$ mice at 3 h after the last injection. ($n = 4$). **k** Quantification of mRNA levels of multiple chemokines in the mixed glial cultures untreated or treated with GDF-15 (100 ng/ml, 6 h). ($n = 4$). **l**, **m** Quantification of CXCL1 and CXCL2 protein levels in the brain tissues of mice at 6 h post intravenous injection with PBS or GDF-15 (2 μg). ($n = 4$, PBS; 5, GDF-15). Error bars, s.e.m. One-way ANOVA with Dunnett post hoc test (**c**, **d**), two-way ANOVA with Bonferroni post hoc test (**e**, **f**, **i**, **j**) and unpaired two-sided Student's *t* test (**k**, **l**, **m**). Source data are provided as a Source Data file.

Moreover, microglia-specific *gain-of-function* NLRP3 mutant-expressing mice exhibited increased *Mmp9* mRNA expression in the brain extracts upon repeated LPS stimulation compared to control mice (Fig. 10h). Intriguingly, recombinant GDF-15 treatment significantly increased MMP9 protein levels (Supplementary Fig. 27a) and *Mmp8* or *Mmp9* mRNA levels in the mixed glial cultures (Supplementary Fig. 27b, c), but much less in BMDMs or neutrophils (Supplementary Fig. 27d–g). Additionally, the pan-MMP inhibitor Ilomastat significantly reduced repeated LPS-induced BBB permeability, as measured by Evans blue and NaF leakage (Fig. 10i–k). These results demonstrate that microglial NLRP3-driven MMPs may play a key role in BBB disruption.

Discussion

As compromised BBB integrity has been recognized as a significant contributor to neuroinflammation and neurological disorders, understanding the cellular processes that control BBB permeability in conditions other than stroke remains a challenge. Previous studies have mainly focused on changes in endothelial cells by examining the expression of tight junction proteins and adhesion molecules in in vitro culture systems[35,36]. To address this limitation, we attempted to elucidate the disruption of BBB integrity by directly observing changes in brain-resident glial cells and brain-infiltrating immune cells within the mouse brain in response to peripheral inflammation. We used repeated intraperitoneal LPS injections to induce peripheral inflammation-mediated BBB disruption. While some previous studies have reported that single or multiple LPS injections do not impair BBB integrity in animal models[37–39], many other studies have used LPS to induce BBB disruption[14,25,40]. To validate our findings, we assessed BBB permeability by measuring the extravascular leakage of various tracers, including Evans blue, NaF and labeled dextran.

Aberrant NLRP3 inflammasome activation has been implicated in the pathogenesis and progression of neurological disorders, including Alzheimer's and Parkinson's diseases[18,19,41]. Although it is still elusive how the deregulated activation of the NLRP3 inflammasome drives neurodegeneration, IL-1β has been considered as a key effector molecule for neurotoxicity and neuroinflammation following inflammasome activation[42–44]. In this context, IL-1β addition has been shown to affect the expression levels of chemokines, adhesion molecules, and tight junction proteins in endothelial cells in vitro[22,35]. However, the direct in vivo effect of inflammasome activation on BBB integrity has not yet been explored in detail. Here, we found that NLRP3 inflammasome mediates peripheral inflammation-triggered BBB disruption, but IL-1β is not required for this NLRP3-dependent BBB impairment. Most importantly, IL-1R deficiency did not attenuate the repeated LPS-induced increases in BBB permeability and myeloid cell infiltration into the brain.

Using a cell-specific NLRP3 hyperactivation model, we identified the important role of microglial NLRP3 inflammasome in transient BBB disruption. Microglia-specific deletion of GSDMD further confirmed the importance of microglial NLRP3-GSDMD signaling axis in this process. For microglia specific expression, we used Tmem119-CreER mice, which are currently considered the most reliable microglial marker. However, given recent findings that TMEM119 can be expressed in certain peripheral cells like follicular dendritic cells[45], we validated microglia specificity using Tmem119-GFP reporter mice. It will be valuable to explore the role of NLRP3-GSDMD axis in other cells during peripheral inflammation-driven BBB disruption in future studies. Our scRNA-seq analysis also indicated that NLRP3 inflammasome activation is unlikely to occur in BBB-comprising non-myeloid cells such as astrocytes and endothelial cells. Supporting these results, astrocyte-specific expression of hyperactive NLRP3 mutant did not enhance the LPS-induced BBB permeabilization. Nonetheless, our scRNA-seq analysis revealed significant gene expression changes in astrocytes in response to NLRP3 activation. NicheNet analysis further showed that astrocyte-microglia communication was markedly enhanced by NLRP3 signaling. Given these findings, the role of astrocytes in LPS-induced BBB disruption warrants further investigation.

The implication of NLRP3 to BBB disruption during intracerebral hemorrhage or stroke model has been proposed[46–48]; however, it remains elusive how NLRP3 activation regulates BBB permeability. In the present study, our data indicate that microglial GSDMD, rather than IL-1R signaling, is necessary for the increased BBB permeability in the context of repeated peripheral inflammation. Of notice, we identified GDF-15 as an NLRP3-GSDMD-dependent secreted protein from microglia. Subsequently, microglial NLRP3-GSDMD activation leads to the production of neutrophil CXCR2-specific chemokines in the BBB-comprising cells possibly via secreting GDF-15. This microglial inflammasome-dependent neutrophil-specific chemokine production may facilitate the strong adhesion of circulating neutrophils to the blood vessels of the brain. Furthermore, both neutrophil depletion and the CXCR2 blockade significantly reduce peripheral inflammation-triggered BBB disruption. These observations suggest that NLRP3-dependent CXCL production and the subsequent neutrophil recruitment into brain vessels are critical phenomenon in the BBB disintegration process (Supplementary Fig. 28).

In agreement with our findings, a recent study proposed a potential role of CXCL1 for herpes simplex virus-1-triggered BBB disruption[49]. Neutrophil infiltration is a major consequence of BBB disruption in the brain pathological conditions. However, our results further support that neutrophil recruitment into the blood vessel can also function as a driver for BBB disruption. Considering that the lifespan of vessel-recruited or brain-infiltrated neutrophils may be less than two or three days, neutrophils may explain the transient BBB disruption in response to LPS-driven peripheral inflammation. Thus, we propose that neutrophil recruitment is a pivotal phenomenon for the BBB disruption process.

https://doi.org/10.1038/s41467-025-56097-1

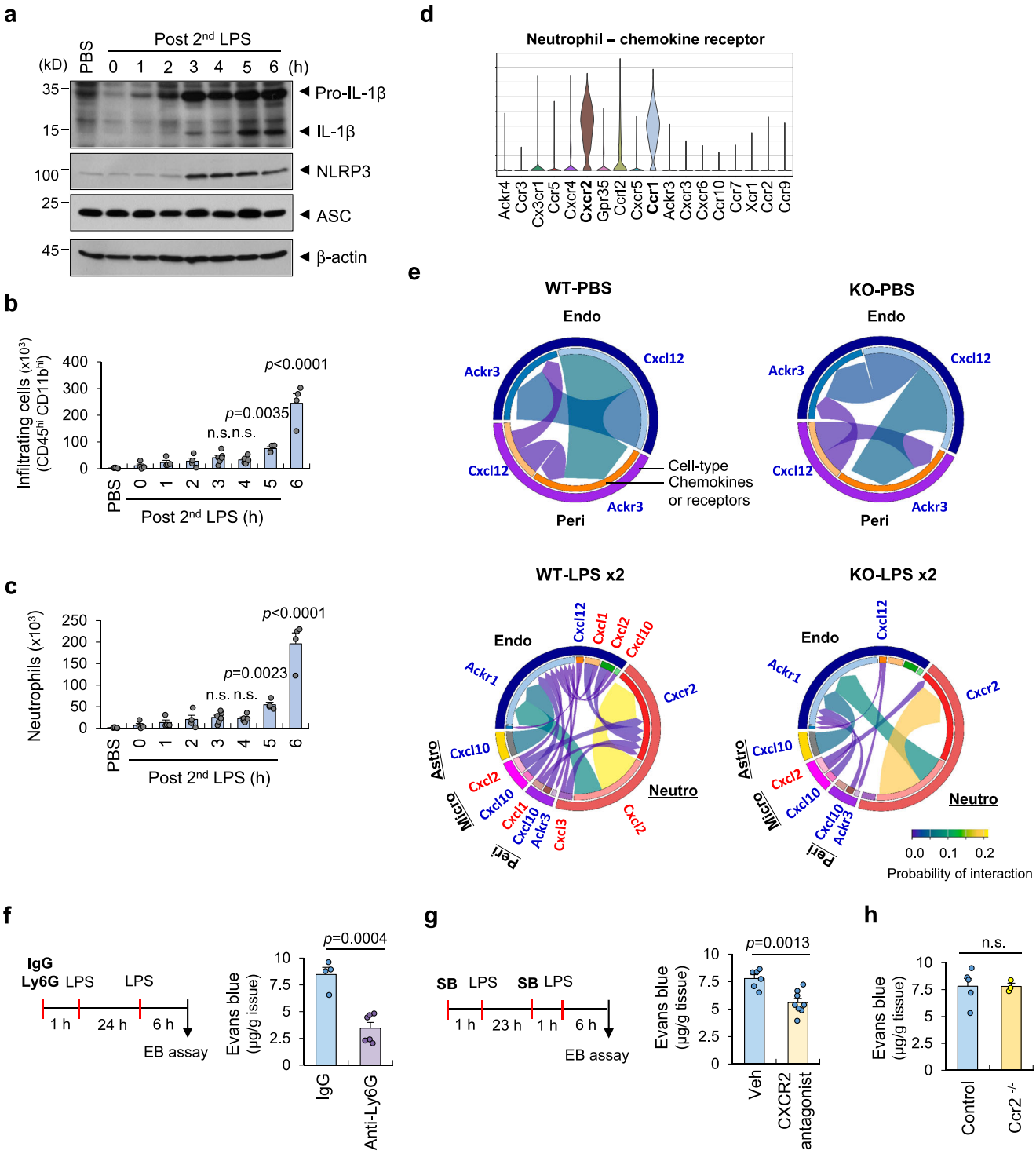

Fig. 9 | Neutrophil recruitment contributes to BBB disruption following peripheral inflammatory stimulation. a Representative immunoblots detecting pro-IL-1β, IL-1β, and NLRP3 in brain lysates of WT mice at different time points (0, 1 - 6 h) after the second LPS injection. **b**, **c** Quantification of brain-infiltrating myeloid cells or neutrophils in the brain of WT mice upon PBS or repeated LPS injection at different time points by flow cytometry. (1 - 6 h post second LPS injection, $n = 5$, PBS, 4 h; 6, 3 h; 4, all other group). **d** Violin plot showing chemokine receptor gene expression in neutrophils of all groups. **e** Circle plot visualizing cell-cell communication in the CXCL signaling pathways for each experimental group. The plot displays interactions among two cell types in the PBS group and 5 cell types (Endo Endothelial cell, Peri Pericyte, Astro Astrocyte, Micro Microglia, Neutro Neutrophil) in the LPS x2 group. The width and color of arrows represent the probability of interaction. **f** Quantification of Evans blue depositions in the WT mouse brains upon repeated LPS injection pretreated with IgG ($n = 4$) or anti-Ly6G ($n = 6$) antibodies (50 μg, *i.p.*) 1 h before 1st LPS injection. **g** Quantification of Evans blue depositions in the WT mouse brains upon repeated LPS injection in the presence of vehicle ($n = 6$) or anti-CXCR2 antagonist SB225002 ($n = 8$) treatment (2 mg/kg, *i.p.*). **h** Quantification of Evans Blue extravasation into the brain followed by LPS injections in WT and *Ccr2*$^{-/-}$ mice. $n = 5$ (WT) or 3 (*Ccr2*$^{-/-}$) mice. Error bars, s.e.m. One-way ANOVA with Dunnett post hoc test (**b**, **c**) and unpaired two-sided Student's *t* test (**f**, **g**, **h**). Source data are provided as a Source Data file.

https://doi.org/10.1038/s41467-025-56097-1

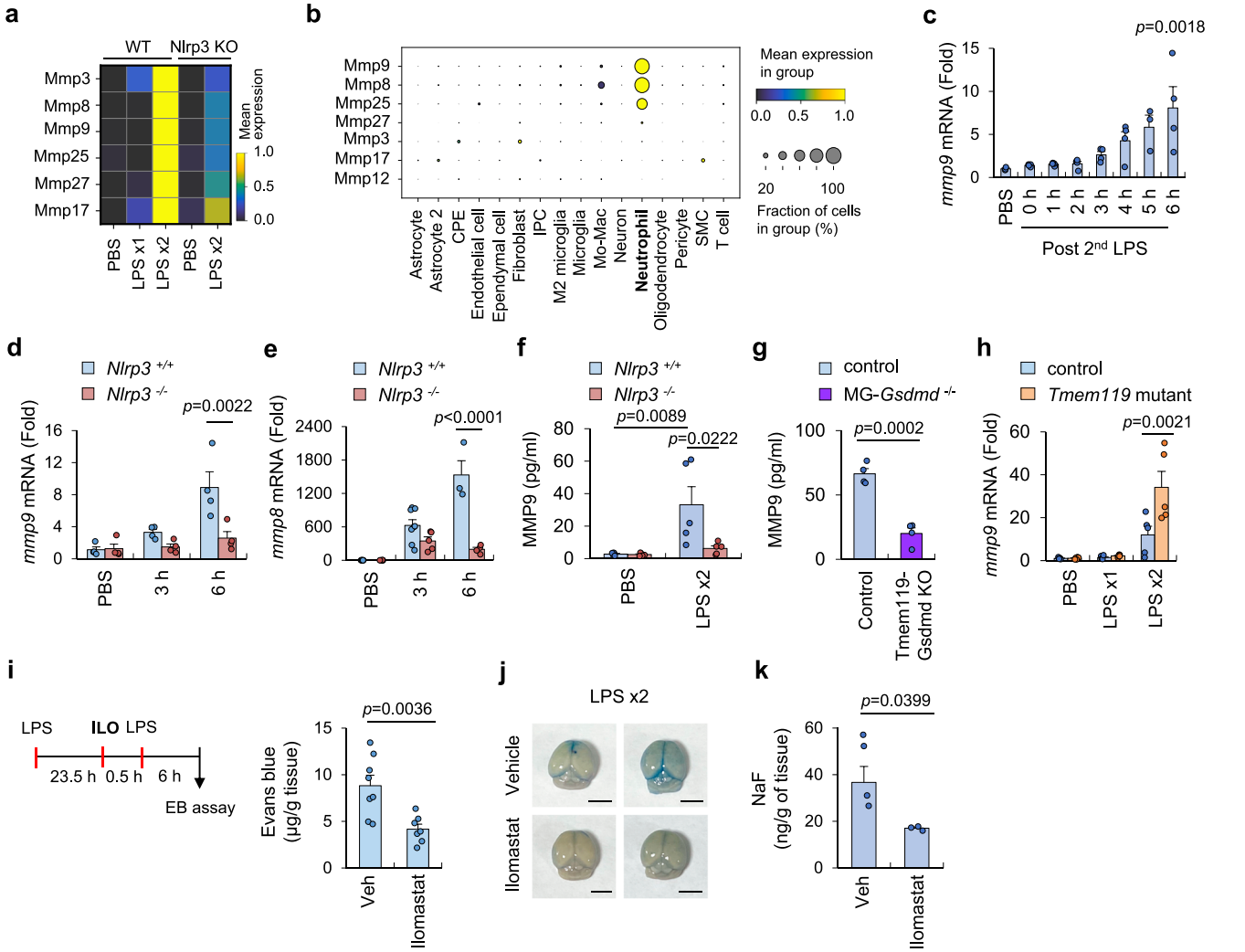

Fig. 10 | NLRP3-GSDMD-dependent upregulation of matrix metalloproteinases and their contribution to BBB disruption. a Heatmap displaying diverse matrix metalloproteinase (MMP) genes in the brain of all clusters of WT and NLRP3 KO mice upon PBS or LPS injection. **b** Dot plot visualizing MMP signaling markers for each cell cluster across all groups. **c** Quantification of brain *Mmp9* mRNA levels in the WT mice at 1 - 6 h post second LPS injection. ($n = 3$, PBS, 5 h; 4, all other group). **d**, **e** Quantification of *Mmp9* or *Mmp8* mRNA levels in the WT and *Nlrp3*$^{-/-}$ mice at 3 or 6 h post second LPS injection. (**d**, $n = 4$; **e**, WT, $n = 5$ for PBS, 8 for 3 h, 3 for 6 h, KO, $n = 5$ for PBS, 3 h, 4 for 6 h). **f**, **g** Quantification of MMP9 levels in the brain extracts of WT and *Nlrp3*$^{-/-}$ (**f**) or microglia-specific *Gsdmd*$^{-/-}$ (**g**) mice at 6 h post repeated LPS injection. ($n = 5$, **f**; $n = 4$, **g**). **h** Quantification of brain mRNA level of *Mmp9* in control and Tmem119-mutant mice ($n = 5$) upon PBS or single/repeated LPS injection at 6 h post last injection. **i** Quantification of Evans bue extravasations in the mouse brains upon repeated LPS injections in the presence of vehicle or MMP inhibitor Ilomastat (50 mg/kg, *i.p.*) at 6 h post 2nd LPS injection. ($n = 8$, Veh, $n = 7$, Ilomastat). **j** Representative images of Evans bue extravasations in the mouse brains following repeated LPS injections in the presence of Ilomastat treatment as in **i**. Scale bars, 0.5 cm. **k** Quantification of NaF extravasations in brain tissues of mice given repeated LPS injections in the presence of Ilomastat. ($n = 4$, Veh, $n = 3$, Ilomastat) Error bars, s.e.m. One-way ANOVA with Dunnett post hoc test (**c**), two-way ANOVA with Bonferroni post hoc test (**d**–**f**, **h**) and unpaired two-sided Student's *t* test (**g**, **i**, **k**). Source data are provided as a Source Data file.

Single cell-based transcriptome analysis revealed that NLRP3 inflammasome activation strongly induced the association of neutrophils with endothelial cells, microglia and pericytes via CXCL signaling. Then, the brain-recruited neutrophils around BBB can exacerbate BBB breakdown by releasing MMP8 or MMP9. Of interest, our results demonstrated that peripheral inflammation-induced MMPs production in the brain is NLRP3-dependent. Moreover, the inhibition of MMPs significantly reduced LPS-induced BBB disruption. Collectively, these findings demonstrate that microglial NLRP3 inflammasome activation leads to the recruitment of neutrophil into the brain and the production of MMPs, which contribute to the BBB disruption. Given the emerging importance of NLRP3 in the brain pathology, NLRP3-dependent BBB disintegration process may be a potent therapeutic target for alleviating neuroinflammation-associated neurological diseases.

Our scRNA-seq analysis revealed that type 1 IFN-related genes and ISGs were specifically upregulated in an NLRP3-dependent manner. However, it remains elusive how type 1 IFN signaling contributes to BBB disruption. IFN signaling has been suggested to contribute to the homeostasis of BBB integrity in certain contexts[50,51]. Therefore, it remains to be further determined whether NLRP3-dependent type 1 IFN signaling may be implicated in BBB disruption during peripheral inflammation.

Despite our findings on microglial NLRP3-dependent BBB disruption, we did not observe robust caspase-1 and GSDMD cleavage in brain tissue immunoblots, although IL-1β cleavage was detected. This discrepancy may be due to differences in antibody sensitivity or insufficient stimulation from repeated intraperitoneal LPS injections, which may not have provided a strong stimulus to induce detectable caspase-1 cleavage. Stronger inflammasome-activating conditions

might reveal such cleavage. Additionally, in our mass spectrometric analysis of microglial secreted proteins, NLRP3-related proteins were not detected under LPS + ATP stimulation. This limitation likely arises from the bottom-up proteomics approach, which involves in-solution proteolytic digestion and peptide fragment matching. Peptide fragments from cleaved caspase-1 or IL-1β may not be accurately recognized as these proteins. This technical limitation might prevent the identification of cleaved caspase-1 or IL-1β as secreted proteins. Furthermore, while we observed no significant sex-dependent differences in LPS-induced brain inflammation phenotypes (Supplementary Fig. 1e, f), most experiments were conducted using mixed populations of male and female mice. For the scRNA-sequencing analysis, each sample was pooled from the brains of two male mice and one female mouse, maintaining this ratio consistently across both the wild-type and *Nlrp3*-deficient groups. However, due to the complexity of our experimental design in the scRNA-seq analysis, the number of replicates was limited to two per group, which represents a limitation of this study.

In conclusion, we validated the critical role of NLRP3-GSDMD axis in peripheral inflammation-driven BBB disruption and proposed a potential effector mechanism of NLRP3 activation in this process. However, the mechanism by which microglial NLRP3 is activated upon repeated peripheral LPS stimulation remains unclear. Through our scRNA-seq analysis, we observed a significant elevation of lipocalin-2 (LCN2), which is considered a potential inflammatory molecule, in the brain. However, our in vitro mixed glial culture experiments revealed that LCN2 is unlikely to activate NLRP3. The molecular mechanisms underlying peripheral LPS-induced microglial NLRP3 activation remain to be clarified in future studies.

Methods

Mice

The protocols for animal experiments were approved by the Institutional Ethical Committee of Yonsei University College of Medicine (2020-0317). All experiments were performed in accordance with the guidelines approved by the Institutional Ethical Committee. C57BL/6, *Nlrp3*^{D301NneoR}, *Cx3cr1*^{creERT}, *Tmem119*^{creERT}, *Aldh1l1*$^{cre/ERT2}$, *Il1r*$^{-/-}$, *Gsdmd*$^{-/-}$ and *Ccr2*$^{-/-}$ mice were obtained from the Jackson Laboratory. *Gsdmd*$^{flox/flox}$ mice were provided by the RIKEN BioResource Research Center. *Rsad2*$^{-/-}$ mice were provided by Dr. Jun-Young Seo (Yonsei University). LysM-GFP mice were provided by Dr. Pilhan Kim (KAIST). *Ifnar1*$^{-/-}$ mice were provided by Dr. Heung Kyu Lee (KAIST). All mice were maintained under specific pathogen-free facility at the Yonsei University College of Medicine with temperature- and humidity-controlled conditions on a 12 h-12 h light-dark cycle. Eight- to twelve-week-old male or female mice were used in the experiments. To generate cell-specific NLRP3 (D301N) mutant expression, *Nlrp3*^{D301NneoR} mice harboring a loxP-flanked neomycin resistance cassette (reverse orientation) in intron 2 and a point mutation in exon 3 of *Nlrp3* were bred into *Cx3cr1*^{creERT}, *Tmem119*^{creERT}, and *Aldh1l1*$^{cre/ERT}$ mice. Mice were treated with tamoxifen (75 mg/kg) for five days to induce active Cre recombinase expression, resulting in the excision of the neomycin resistance cassette and the expression of NLRP3 (D301N) in Cx3cr1-, Tmem119-, and Aldh1l1-specific cells. *Gsdmd*$^{flox/flox}$ mice were bred with *Tmem119*^{creERT} mice to generate microglia-specific *Gsdmd*-deficient mice. We analyzed the potential sex-dependent effect on repeated LPS-induced BBB permeability and found no significant differences. Most experiments were conducted using mixed populations of male and female mice. The number of male and female mice used in each experiment was provided in Source Data.

Mice treatment

To induce peripheral inflammation, mice were given intraperitoneal injection with lipopolysaccharides (LPS, 0.8 mg/kg) once or twice at 24 h intervals. Alternatively, mice were given intravenous injection with cytokine cocktail of IL-1β (10 μg/kg), IL-6 (35 μg/kg) and TNFα (35 μg/kg) three times at 6 h or 18 h intervals to induce peripheral inflammation. To block NLRP3 inflammasome-mediated signaling, mice were administered MCC950 (10 mg/kg) or an IL-1 receptor antagonist (10 mg/kg) 30 min prior to LPS injection. Mice were anesthetized with isoflurane, transcardially perfused with PBS (20 ml), and the brain tissues were isolated after removing olfactory regions, brainstem, and meninges[52]. These whole brain tissues were used for most experiments including BBB permeability assay, flow cytometric analysis, immunoblotting, quantitative real-time PCR and enzyme-linked immunosorbent assay.

BBB permeability assay

BBB integrity was assessed by measuring the extravascular leakage of Evans blue, sodium fluoride and fluorescently-labeled dextran into brain parenchyma. Mice were intravenously injected with Evans blue (0.2 mg/kg) or sodium fluoride (11 mg/kg) via the tail vein. After 1 h, under deep anesthesia with isoflurane, mice were perfused with PBS and brain tissues were collected. For Evans blue quantification, brain tissues were homogenized in saline using dounce grinder, extracted with trichloroacetic acid, and fluorescence was measured at 620 nm excitation/680 nm emission 680 nm using a Varioskan Flash 3001 microplate fluorometer (Thermo Fisher). Sodium fluoride was quantified by homogenizing brain tissues in 1 % Triton-X 100 in PBS, and fluorescence was measured at 492 nm excitation/525 nm emission. BBB permeability was further evaluated by measuring the leakage of Texas red-conjugated dextran (70 kDa). Dextran (1 mg) was administered via the tail vein 1 h before euthanization with isoflurane, and brain tissue was analyzed using immunohistochemical analyses to quantify dextran leakage.

Flow cytometry

Harvested brains were homogenized in RPMI-1640 medium containing DNase I and collagenase IV using a Dounce homogenizer. The homogenates were filtered through a cell strainer (70 μm), subjected to a 30% Percoll gradient to remove myelin debris, and a single-cell suspension was used for flow cytometry analysis. The cells were stained with fluorochrome-conjugated monoclonal antibodies against CD45 (BioLegend, 103116), CD11b (Invitrogen, 12-0112-82), Ly6C (Invitrogen, 53-5932-82), and Ly6G (Invitrogen, 17-9668-82). The dead cells were excluded with 4′,6-diamidino-2-phenylindol (DAPI) (Invitrogen, D1306) counterstaining. Analyses were performed using a FACSVerse (BD Biosciences) and FlowJo software (TreeStar).

Immunohistochemistry

Mice were anesthetized with isoflurane and transcardially perfused with PBS and 4% paraformaldehyde. The brain tissue was post-fixed in 4% PFA overnight at 4 °C, and then placed in 30% sucrose until the sample sank to the bottom for dehydration. The brain tissues were embedded in OCT compound and coronally sectioned into 30 μm thick slices using a Leica CM1860 cryostat. Brain sections were permeabilized with 0.3% Triton X-100 for 30 min and blocked with a 4% BSA solution for 1 h at room temperature (RT). The sections were incubated with anti-GFAP (Invitrogen, PA1-10004, 1:2000) and anti-Iba1 (Wako, 019-19741, 1:500) antibodies in 1% BSA overnight at 4 °C, followed by secondary antibody staining for 3 h at RT. The sections were labeled with DAPI to visualize the nuclei. The sections were then mounted using mounting solution (Invitrogen, P36934) and covered with a coverslip. Images were acquired using a confocal microscope (LSM980, Carl Zeiss) and processed using Zen Blue software. The mean fluorescence intensity (MFI), cell counts, and microglial morphology were quantified using ImageJ software and Imaris v.9.7.

Two-photon intravital microscopy

For intravital imaging of the murine brain using a two-photon microscope, the surgical procedure of cranial window implantation was performed as described previously[53]. Briefly, the mice were anesthetized with Zoletil and positioned on a customized stereotactic stage atop a 37 °C heating pad (Live Cell Instruments). Hair was removed from the frontal and parietal skull regions. A cranial window was created using a microdrill to form a circle of approximately 4 mm in the parietal bone of the skull. The exposed cerebral cortex was then covered with a 5 mm round cover glass using tissue glue. After one hour for recovery, the mice were then intravenously (i.v.) injected with 10 kDa or 70 kDa Texas Red-dextran (500 μg) and placed on a custom-built microscopy platform for imaging. To track and quantify vascular permeability, the post-capillary venules of the right parietal cortex of mice were imaged for over 20 min with 1 μm optical sections. Images were analyzed using Volocity software (PerkinElmer). Vascular permeability was quantified as the intensity of 10 kDa Texas Red-tagged dextran observed outside the vessel surface, as described previously[14].

Ex vivo active caspase-1 detection

The Cy5.5- and BHQ-3 conjugated active caspase-1 probes were provided by Dr. Ju Hee Ryu (KIST). To detect active caspase-1 activity in organs, the caspase-1-specific probe (100 μg/ mouse) was i.v. administered via tail vein 1 h before euthanization with isoflurane. For ex vivo imaging, each organ was collected after transcardial perfusion with PBS. Cy5.5 fluorescence, produced only in the presence of active caspase-1, in the isolated organs was analyzed using an IVIS Spectrum In Vivo imaging system (PerkinElmer).

Immunoblot analysis

Brain tissues were lysed in a buffer containing 20 mM HEPES (pH 7.5), 0.5% Nonidet P-40, 50 mM KCl, 150 mM NaCl, 1.5 mM $MgCl_2$, 1 mM EGTA, and protease inhibitors. Soluble lysates were fractionated using sodium dodecyl sulfate-polyacrylamide gel electrophoresis (SDS-PAGE) and transferred to polyvinylidene fluoride (PVDF) membranes. The membranes were then stained with appropriate primary and horseradish peroxidase (HRP)-conjugated secondary antibodies. All blots are representative images from at least three independent experiments.

Reagents and antibodies

LPS (L3012), MCC950 (PZ0280), tamoxifen (T5648), sodium fluoride (NaF, F6377), and Evans blue (E2129) were purchased from Sigma-Aldrich. IL-1 receptor antagonist (cyt-203) was obtained from ProSpec. Recombinant cytokines and proteins were purchased as follows: IL-1β (Thermo Fisher Scientific, 211-11B), IL-6 (Thermo Fisher Scientific, 216-16), TNFα (Thermo Fisher Scientific, 315-01 A), and GDF-15 (prospec, CYT-857). CXCR2 antagonist SB225002 (S7651) was obtained from Selleckchem. MMP inhibitor Ilomastat (HY-15768) was purchased from MedChemExpress. Texas red-conjugated dextran (D1830, D1828) was purchased from Thermo Fisher Scientific. Cy3-(712-165-050) and Alexa Fluor 488-conjugated (712-545-150) anti-rat IgG antibodies were purchased from Jackson ImmunoResearch. Anti-mouse caspase-1 (AG-20B-0042, 1:1000) and anti-NLRP3 (AG-20B-0014, 1:1000) antibodies were obtained from AdipoGen. Anti-mouse IL-1β antibody (AF-401-NA, 1:2000) was obtained from R&D Systems. Anti-ASC (SC-22514-R, 1:500) and anti-β-actin (SC-47778, 1:500) was purchased from Santa Cruz Biotechnology. Anti-GSDMD antibody (209845, 1:1000) was obtained from Abcam. All flow cytometry antibodies were validated in our laboratory based on the manufacturer's websites. All immunohistochemistry antibodies were validated using the secondary antibodies alone control. All immunoblotting antibodies were validated in each gene-specific knockout bone marrow-derived macrophages.

Enzyme-linked immunosorbent assay (ELISA)

Whole blood samples were collected and centrifuged for serum isolation, and the serum samples were diluted for ELISA. For brain tissue lysates, the brain was homogenized in a buffer containing 10 mM Tris-Cl (pH 7.4), 2 mM EDTA, 150 mM NaCl, and protease inhibitors (TEN buffer) using a Dounce tissue grinder. The supernatants were collected after centrifugation and subjected to Bradford assay for protein quantification. The concentrations of IL-1β, IL-6, IL-18, CXCL1, CXCL2, and MMP9 were measured using the ELISA DuoSets kit (R&D Systems) according to the manufacturer's instructions.

Quantification of mRNA

Total RNA was isolated from brain tissues using TRIzol reagent (Invitrogen), and then was reverse transcribed using the Reverse Transcriptase primer mix (Takara). Quantitative real-time PCR was performed using SYBR Premix Ex Taq (Takara) for comparative analysis of gene expression, in which Rn18s was amplified as the control gene. Primers were as follows: 5′-GCC CAT CCT CTG TGA CTC AT-3′ and 5′-AGG CCA CAG GTA TTT TGT CG-3′ (*Il1b)*; 5′-AGT TGC CTT CTT GGG ACT GA-3′ and 5′-TCC ACG ATT TCC CAG AGA AC-3′ (*Il6*); 5′-GCT GGG ATT CAC CTC AAG AA-3′ and 5′-TGG GGA CAC CTT TTA GCA TC-3′ (*Cxcl1*); 5′-GTT TCT GGG GAG AGG GTG AG-3′ and 5′-TGT TCT ACT CTC CTC GGT GC-3′ (*Cxcl2*); 5′- AGA CCA TCC AGA GCT TGA CG-3′ and 5′-GGA CTT GCC GCT CTT CAG TA-3′ (*Cxcl3*); 5′-TTC CTC AGT CAT AGC CGC AA-3′ and 5′-TGG ATC CAG ACA GAC CTC CT-3′ (*Cxcl5*); 5′-CCG AAG CAA ACA TCA CAT TCA-3′ and 5′-GGT CTA AAG GCT CCG GGC T-3′ (*Inos*); 5′-CCA CCA GCA GAC AGT GTT TC-3′ and 5′-GAA GAT CTC TGC TCG GAC CA-3′ (*Ifnb1*); 5′-CCT CTG CTT TCT AGT GAT GCC G-3′ and 5′-CGT AAA CAC GGT CTT GCT CCT G-3′ (*Irf7*); 5′-CTT CAA CGT GGA CGA AGA CA-3′ and 5′-ATT CAG GCA CCA AAC AGG AC-3′ (*Rsad2*); 5′- AGG TGT CCC AAA GAA GCT GT-3′ and 5′- ACA GAA GTG CTT GAG GTG GT-3′ (*Ccl2*); 5′- GCC ATA GTC TTC AAG ACC AAG CTT-3′ and 5′- TGG CAT CCT GGA CCC ACT T-3′ (*Ccl11*); 5′- CAA ACT GGG CAA GGA GAT CTG-3′ and 5′- GGC CCA GGT GTT TCA TAT AAT TCT-3′ (*Ccl13*); 5′- GCA GAT CCC CAG AAA CTG AG-3′ and 5′- GGC ACC AGG ACG TAT GAG TT-3′ (*Cx3cl1*); 5′- TCG CCT GAA GAC ACT TCC AT-3′ and 5′- GCG CTG CAT CTC TTT AAG CT-3′ (*Mmp8*); 5′- CTT CTG GCG TGT GAG TTT CCA-3′ and 5′- ACT GCA CGG TTG AAG CAA AGA-3′ (*Mmp9*); 5′- GAC ATC ACT AGG CCC CTG AA-3′ and 5′- TTC AAG AGT TGC CTG CAC AG-3′ (*Gdf-15*); 5′-CGC GGT TCT ATT TTG TTG GT-3′ and 5′-AGT CGG CAT CGT TTA TGG TC-3′ (*Rn18s*).

Cell cultures

Mouse brain mixed glial cells were prepared from the whole brains of mouse pups on postnatal days 1–3 and cultured for three weeks. Mixed glial cells and microglia were cultured in Dulbecco's Modified Eagle Medium/Nutrient Mixture F-12 (DMEM/F12, 1:1) supplemented with 10% fetal bovine serum (FBS) and antibiotics. Murine bone marrow cells were isolated from the femurs and tibias of mice and cultured in L929-conditioned DMEM for 5 days to differentiate into bone-marrow-derived macrophage (BMDMs)[54]. BMDMs were maintained in L929-conditioned DMEM supplemented with 10% FBS and antibiotics.

Detection of MCC950 delivery into the brain

Mice were intraperitoneally injected with PBS or MCC950 (10 mg/kg). Six hours post injection, mouse brains were isolated as described above, homogenized and lysed with RIPA buffer. Soluble lysates were further extracted with MTBE and reconstituted in a solvent mixture of formic acid and acetonitrile. A liquid chromatography-tandem mass spectrometry (LC-MS/MS) method was developed for MCC950 detection using negative-mode electrospray ionization (ESI) with an MCC950 standard. The analysis was performed using a ThermoFisher Vanquish UHPLC coupled to a TSQ Altis mass spectrometer using a C18 column. Gradient elution was carried out using a mobile phase consisting of 0.1% formic acid in deionized water and acetonitrile.

Quantitative detection was achieved through multiple reaction monitoring (MRM) with a transition of m/z 403 → 204, corresponding to the loss of sodium (Na^+) from MCC950 sodium (exact mass: 426.122).

Secretome analysis by mass spectrometry

To identify NLRP3-GSDMD-specific secreted proteins, WT and *Gsdmd*-deficient microglia were isolated from the primary mixed glial cell cultures by shaking (200 rpm, 4 h). Microglia were then treated with LPS (0.25 μg/ml, 3 h), followed by ATP treatment (2.5 mM, 20 min), or treated with ATP alone. Cell-free supernatants from WT and *Gsdmd*-deficient microglia were then analyzed by mass spectrometry. To prepare proteins for digestion, each cell supernatant (140 μl) was mixed with 100 mM triethylammonium bicarbonate (TEAB) buffer (60 μl, pH 8.5). Subsequently, the mixture was subjected to reduction using 200 mM Tris 2-carboxyethyl phosphine (TCEP) for 1 h at 55 °C, followed by alkylation with 375 mM iodoacetamide (IAA) for 30 min in the absence of light. Clean protein pellets were obtained by acetone precipitation, reconstituted in 100 mM TEAB buffer, and subjected to trypsin digestion at 37 °C for 16 h. The resulting peptide mixture was then labeled using the TMT 10plex™ isobaric mass tagging kit reagent (Thermo Fisher Scientific) according to the manufacturer's guidelines for accurate relative quantification. After vacuum drying, the samples were desalted using peptide desalting spin columns (Thermo Fisher Scientific), followed by re-drying and suspension in 0.1% formic acid. Analysis was performed using a Dionex Ultimate 3000 RSLC nano-HPLC system coupled to an Orbitrap Q Exactive mass spectrometer (Thermo Fisher Scientific). Quantification and normalization were conducted with Proteome Discoverer 2.3 software (Thermo Fisher Scientific).

Neutrophil depletion

For neutrophil depletion, mice were intraperitoneally injected with anti-mouse Ly6G (Bio X Cell, BE0075-1) or control IgG (Bio X Cell, BE0089) antibodies (50 μg/mouse) 1 h prior to the first LPS injection. Mouse brain tissues were harvested 6 h after the second injection of LPS. To confirm neutrophil depletion, blood samples were collected 6 h after the last LPS injection (LPS ×2), and the populations of neutrophils ($CD45^+$, $CD11b^+$, $Ly6G^+$) and monocytes ($CD45^+$, $CD11b^+$, $Ly6C^+$, $Ly6G^-$) were analyzed using flow cytometry.

Single cell isolation for scRNA-sequencing

After transcardial perfusion, murine brain tissue was enzymatically dissociated into single-cell suspensions using an Adult Brain Dissociation Kit (130-107-677, Miltenyi Biotec) according to the manufacturer's instructions. The dissociated samples were collected and filtered through a 70 μm cell strainer. Myelin debris was removed using a debris removal solution, and red blood cell (RBC) lysis was performed using an RBC removal solution. Hemispheres from three mice (two male and one female) were pooled into one single replicate for each group (PBS, LPS ×1, LPS ×2) of both WT and *Nlrp3*$^{-/-}$ mice.

Library preparation and single-cell transcriptomic analysis

Libraries were prepared using the chromium controller according to the 10X chromium Next GEM Single Cell 3' v3.1 protocol (CG000315). Briefly, single-cell suspensions were diluted in nuclease-free water to obtain samples with a cell count of 10,000. Equally counted cell suspensions were loaded onto a chromium Next GEM chip. RNA transcripts from single cells were barcoded and reverse-transcribed. After processing, the products were purified and enriched using polymerase chain reaction (PCR) to create the final cDNA library. The resulting libraries were quantified using qPCR according to the qPCR Quantification Protocol Guide and qualified using an Agilent Technologies 4200 TapeStation. The libraries were finally sequenced using the HiSeq platform (Illumina) according to the read length specified in the user guide.

Single-cell transcriptomics were analyzed using Cell Ranger v7.1.0 (10x Genomics). Briefly, FASTQ files were generated by demultiplexing the raw BCL files from the Illumina sequencing instrument using the 'cellranger mkfastq' tool. Subsequently, the raw FASTQ files underwent further processing with the 'cellranger count' tool. This step involved mapping to the mouse reference genome (mm10-2020-A), quantifying gene expression using unique molecular identifiers (UMIs), identifying cell clusters, and performing differentially expressed gene (DEG) analysis. The final dataset was generated by aggregating multiple independent samples using "cellranger aggr." The analysis was conducted using the Python package, Scanpy. Cell clustering and UMAP analyses were performed based on statistically significant principal components. DEGs between the control and experimental groups were determined using the Wilcoxon rank-sum test, with the '-FindMarkers' function in Scanpy. The false discovery rate (FDR) was controlled using adjusted p-values and Bonferroni corrections. Gene enrichment and functional annotation analyses for the significant probe list were performed using g:Profiler (https://biit.cs.ut.ee/gprofiler/).

Single cell RNA-sequencing analysis of the whole brain transcriptome

Quality control and data analysis. The doublet removal process was conducted on the dataset acquired using Scrublet software. Cells with <500 unique transcripts were eliminated, and those with >20% of the transcripts mapping to mitochondrial genes were filtered out. Cells displaying a unique gene count of >8500 genes were considered outliers and discarded, resulting in the removal of 19,243 cells. Counts data underwent log-normalization utilizing the pp.normalize function, and were processed with pp.highly_variable_gene with the flavor "seurat_v3" incorporating 2000 genes. The number of principal components was set to 40 for the tl.umap function. Batch correction was performed using the Harmony algorithm for each sample to reduce batch effects between samples.

Identifying marker genes and evaluating cluster identity. To characterize the clusters obtained from the Harmony-corrected object, we conducted differential expression analysis between the clusters and classified them based on putative marker gene expression. Gene set scoring was performed using VISION scoring with the inflammasome gene sets, as shown in Fig. 4e. We used the tl.rank_genes_groups function to generate rankings for the DEGs in each cluster, followed by comparison with the rest of the cells using the Wilcoxon Rank-sum test corrected by the Benjamini–Hochberg correction. Visualization of specific marker genes was achieved using a pl. matrix plot.

Gene-set enrichment analysis (GSEA). Gene set enrichment analysis was conducted using Gprofiler-official version 1.0.0[55] and GSEApy. Differential gene analysis was conducted using tl.rank_genes_groups Wilcoxon Rank-sum tests with tie-correction, and the results were presented as percentages. The reference datasets included WikiPathways_2019_Mouse, MSigDB_Hallmark_2020, Gene Ontology: Biological Processes_2023, and Molecular Function_2023. Filtered DEGs were obtained for endothelial cells, pericytes, astrocytes, and microglia by comparing WT PBS vs. LPS ×2, with a p-value < 0.05, and log-fold changes >1 were used ($Log_2FC = 2$). When comparing WT LPS ×2 and NLRP3 KO type LPS ×2, DEGs were analyzed in astrocytes and microglia using the same criteria. However, for endothelial cells, DEGs were calculated with a p-value cutoff of 0.05 and a minimum log_2FC of 0.5. For pericytes, DEGs were calculated using a minimum log_2FC of 0.5. DEGs analysis of the entire cell population comparing WT-PBS vs. LPS ×2 and WT-LPS ×2 vs. KO-LPS ×2 utilized parameters, including a p-value cutoff of 0.05, a percent non-zero from reference <50%, a percent non-zero group fraction >25%, and log fold changes >0.58.

Microglia subset analysis. To analyze microglia-specific subsets, we isolated the microglia clusters from the main dataset for focused examination. After subsetting, we identified specific gene markers and evaluated their expression levels based on varying Leiden resolutions (Leiden 1.7). This process yielded 10 distinct clusters. Each cluster was annotated according to its unique gene marker profile. Through this approach, we categorized the microglia into 6 subclusters, providing a more granular understanding of microglial diversity and functional specialization within the dataset.

Cell-cell communication analysis. To explore intercellular communication networks, we used CellChat (v.1.6.1), a computational tool for predicting ligand-receptor interactions. This analysis required two primary inputs: the gene expression data of cells and the assigned cell labels. Using these data, we created a CellChat object and applied CellChatDB to calculate communication probabilities between cell types. The results were organized into a data frame, generating figures that highlight signaling pathways and intercellular interactions specific to each condition.

To investigate upregulated interactions in astrocyte, astrocyte2, and microglia under WT and NLRP3 KO LPS x2 conditions, we performed ligand-receptor analysis using NicheNet (v2.1.5) on these cell clusters. Differential gene expression analysis was conducted as follows:

1. Intra-subset comparisons: Using pyDESeq2, we compared WT and N3KO LPS x2 conditions in scRNA-seq data.
2. Inter-subset comparisons: We applied the Scanpy tl.rank_genes_groups function, using the 'wilcoxon' method with tie correction for single-cell level differential testing.

Gene sets for NicheNet were selected using differential expression criteria: adjusted *P*-value < 0.05, absolute log-fold change >log2(1.5), and a within-group expression fraction >0.1. Condition-specific ligand-receptor pairs were identified when both the prioritization score and expression product fold-changes exceeded 4. The top 30 interactions, based on expression product fold-change, revealed significant communication pathways.

scFates for trajectory analysis. To analyze the trajectory within the microglia, we initially subsetted this cell type and then computed the principal component analysis representation of the data matrix using the sc.pp.neighbors function. The neighborhood graph was then embedded using UMAP via the tl.umap function after using the sc.tl.diffmap function. By identifying connecting nodes between clusters, we established a trajectory within microglial subclusters, defining three overarching routes. DEG analysis was performed to identify the specific marker genes for each trajectory route. The resulting marker genes were visually represented using a pl. matrix plot. This comprehensive approach allowed us to delineate distinct routes within microglia and characterize the unique molecular signatures associated with each trajectory, thus providing valuable insights into the transcriptional dynamics of microglial subclusters.

Statistical analysis

All values are expressed as the mean and standard error of the mean (s.e.m.). The number of animals in each experimental group is shown in the legend of each figure. Data were analyzed using unpaired two-tailed Student's *t* test, one-way analysis of variance (ANOVA) followed by Dunnett's post hoc test, or two-way ANOVA with the Bonferroni post hoc test. The level of statistical significance was set at $P \leq 0.05$. All statistical analyses were performed using GraphPad Prism 8.0.

Reporting summary

Further information on research design is available in the Nature Portfolio Reporting Summary linked to this article.

Data availability

Single-cell RNA-sequencing data generated in this study have been deposited in Gene Expression Omnibus (GEO) under accession number GSE263094. Based on this dataset, the differentially expressed genes (DEGs) for each group has been provided in the Supplementary Data 1. Mass spectrometry proteomics data generated in this study have been deposited to the ProteomeXchange Consortium via the PRIDE partner repository with the dataset identifier PXD051438. Any additional data are available within the article and Supplementary Information files. Source data are provided with this paper.

References

1. Abbott, N. J., Ronnback, L. & Hansson, E. Astrocyte-endothelial interactions at the blood-brain barrier. *Nat. Rev. Neurosci.* **7**, 41–53 (2006).
2. Xiao, M., Xiao, Z. J., Yang, B., Lan, Z. & Fang, F. Blood-Brain Barrier: More Contributor to Disruption of Central Nervous System Homeostasis Than Victim in Neurological Disorders. *Front. Neurosci.* **14**, 764 (2020).
3. Galea, I. The blood-brain barrier in systemic infection and inflammation. *Cell. Mol. Immunol.* **18**, 2489–2501 (2021).
4. Bernardo-Castro, S. et al. Pathophysiology of Blood-Brain Barrier Permeability Throughout the Different Stages of Ischemic Stroke and Its Implication on Hemorrhagic Transformation and Recovery. *Front. Neurol.* **11**, 594672 (2020).
5. Qiu, Y. M. et al. Immune Cells in the BBB Disruption After Acute Ischemic Stroke: Targets for Immune Therapy? *Front. Immunol.* **12**, 678744 (2021).
6. Sweeney, M. D., Sagare, A. P. & Zlokovic, B. V. Blood-brain barrier breakdown in Alzheimer disease and other neurodegenerative disorders. *Nat. Rev. Neurol.* **14**, 133–150 (2018).
7. van Vliet, E. A., Aronica, E. & Gorter, J. A. Blood-brain barrier dysfunction, seizures and epilepsy. *Semin. Cell Dev. Biol.* **38**, 26–34 (2015).
8. Arvanitis, C. D., Ferraro, G. B. & Jain, R. K. The blood-brain barrier and blood-tumour barrier in brain tumours and metastases. *Nat. Rev. Cancer* **20**, 26–41 (2020).
9. Zhang, L. et al. SARS-CoV-2 crosses the blood-brain barrier accompanied with basement membrane disruption without tight junctions alteration. *Sig. Transduct. Target Ther.* **6**, 337 (2021).
10. Chen, Y., Yang, W., Chen, F. & Cui, L. COVID-19 and cognitive impairment: neuroinvasive and blood–brain barrier dysfunction. *J. Neuroinflammation* **19**, 222 (2022).
11. Greene, C., et al. Blood-brain barrier disruption and sustained systemic inflammation in individuals with long COVID-associated cognitive impairment. *Nat. Neurosci.* **27**, 421–432 (2024).
12. Kikuchi, D. S. et al. Poldip2 mediates blood-brain barrier disruption in a model of sepsis-associated encephalopathy. *J. Neuroinflammation* **16**, 241 (2019).
13. Huang, X., Hussain, B. & Chang, J. Peripheral inflammation and blood-brain barrier disruption: effects and mechanisms. *CNS Neurosci. Ther.* **27**, 36–47 (2021).
14. Haruwaka, K. et al. Dual microglia effects on blood brain barrier permeability induced by systemic inflammation. *Nat. Commun.* **10**, 5816 (2019).
15. Swanson, K. V., Deng, M. & Ting, J. P. The NLRP3 inflammasome: molecular activation and regulation to therapeutics. *Nat. Rev. Immunol.* **19**, 477–489 (2019).
16. Keyel, P. A. How is inflammation initiated? Individual influences of IL-1, IL-18 and HMGB1. *Cytokine* **69**, 136–145 (2014).
17. Heneka, M. T. et al. NLRP3 is activated in Alzheimer's disease and contributes to pathology in APP/PS1 mice. *Nature* **493**, 674–678 (2013).
18. Ising, C. et al. NLRP3 inflammasome activation drives tau pathology. *Nature* **575**, 669–673 (2019).

19. Lee, E. et al. MPTP-driven NLRP3 inflammasome activation in microglia plays a central role in dopaminergic neurodegeneration. *Cell Death Differ.* **26**, 213–228 (2019).
20. Fan, Z. et al. Systemic activation of NLRP3 inflammasome and plasma alpha-synuclein levels are correlated with motor severity and progression in Parkinson's disease. *J. Neuroinflammation* **17**, 11 (2020).
21. Jang, J. et al. 25-hydroxycholesterol contributes to cerebral inflammation of X-linked adrenoleukodystrophy through activation of the NLRP3 inflammasome. *Nat. Commun.* **7**, 13129 (2016).
22. Labus, J., Hackel, S., Lucka, L. & Danker, K. Interleukin–1beta induces an inflammatory response and the breakdown of the endothelial cell layer in an improved human THBMEC-based in vitro blood-brain barrier model. *J. Neurosci. Methods* **228**, 35–45 (2014).
23. Zhou, X. et al. Aspirin alleviates endothelial gap junction dysfunction through inhibition of NLRP3 inflammasome activation in LPS-induced vascular injury. *Acta Pharm. Sin. B* **9**, 711–723 (2019).
24. Bellut, M. et al. NLPR3 inflammasome inhibition alleviates hypoxic endothelial cell death in vitro and protects blood-brain barrier integrity in murine stroke. *Cell Death Dis.* **13**, 20 (2021).
25. Wendeln, A. C. et al. Innate immune memory in the brain shapes neurological disease hallmarks. *Nature* **556**, 332–338 (2018).
26. Biswas, S. K. & Lopez-Collazo, E. Endotoxin tolerance: new mechanisms, molecules and clinical significance. *Trends Immunol.* **30**, 475–487 (2009).
27. Ko, Y. J. et al. Non-invasive in vivo imaging of caspase-1 activation enables rapid and spatiotemporal detection of acute and chronic inflammatory disorders. *Biomaterials* **226**, 119543 (2020).
28. Sansonetti, P. J. et al. Caspase-1 activation of IL-1beta and IL-18 are essential for Shigella flexneri-induced inflammation. *Immunity* **12**, 581–590 (2000).
29. Shi, J. et al. Cleavage of GSDMD by inflammatory caspases determines pyroptotic cell death. *Nature* **526**, 660–665 (2015).
30. Ma, J. H. et al. Therapeutic effect of NLRP3 inhibition on hearing loss induced by systemic inflammation in a CAPS-associated mouse model. *EBioMedicine* **82**, 104184 (2022).
31. Neven, B. et al. Molecular basis of the spectral expression of CIAS1 mutations associated with phagocytic cell-mediated autoinflammatory disorders CINCA/NOMID, MWS, and FCU. *Blood* **103**, 2809–2815 (2004).
32. Konrad, F. M. & Reutershan, J. CXCR2 in acute lung injury. *Mediators Inflamm.* **2012**, 740987 (2012).
33. de Almeida, L. G. N. et al. Matrix Metalloproteinases: From Molecular Mechanisms to Physiology, Pathophysiology, and Pharmacology. *Pharmacol. Rev.* **74**, 712–768 (2022).
34. Rempe, R. G. et al. Matrix Metalloproteinase-Mediated Blood-Brain Barrier Dysfunction in Epilepsy. *J. Neurosci.* **38**, 4301–4315 (2018).
35. Wang, J. G. et al. Monocytic microparticles activate endothelial cells in an IL-1beta-dependent manner. *Blood* **118**, 2366–2374 (2011).
36. Bai, B. et al. NLRP3 inflammasome in endothelial dysfunction. *Cell Death Dis.* **11**, 776 (2020).
37. Chen, Z. et al. Neuroprotection by Preconditioning in Mice is Dependent on MyD88-Mediated CXCL10 Expression in Endothelial Cells. *ASN Neuro* **15**, 17590914221146365 (2023).
38. Wang, P. et al. Systemic injection of low-dose lipopolysaccharide fails to break down the blood-brain barrier or activate the TLR4-MyD88 pathway in neonatal rat brain. *Int. J. Mol. Sci.* **15**, 10101–10115 (2014).
39. Bickel, U., Grave, B., Kang, Y. S., del Rey, A. & Voigt, K. No increase in blood-brain barrier permeability after intraperitoneal injection of endotoxin in the rat. *J. Neuroimmunol.* **85**, 131–136 (1998).
40. Thomson, C. A., McColl, A., Graham, G. J. & Cavanagh, J. Sustained exposure to systemic endotoxin triggers chemokine induction in the brain followed by a rapid influx of leukocytes. *J. Neuroinflammation* **17**, 94 (2020).
41. Milner, M. T., Maddugoda, M., Gotz, J., Burgener, S. S. & Schroder, K. The NLRP3 inflammasome triggers sterile neuroinflammation and Alzheimer's disease. *Curr. Opin. Immunol.* **68**, 116–124 (2021).
42. Sutton, C., Brereton, C., Keogh, B., Mills, K. H. & Lavelle, E. C. A crucial role for interleukin (IL)-1 in the induction of IL-17-producing T cells that mediate autoimmune encephalomyelitis. *J. Exp. Med.* **203**, 1685–1691 (2006).
43. Levesque, S. A. et al. Myeloid cell transmigration across the CNS vasculature triggers IL-1beta-driven neuroinflammation during autoimmune encephalomyelitis in mice. *J. Exp. Med.* **213**, 929–949 (2016).
44. Mendiola, A. S. & Cardona, A. E. The IL-1beta phenomena in neuroinflammatory diseases. *J. Neural Transm.* **125**, 781–795 (2018).
45. Vankriekelsvenne, E. et al. Transmembrane protein 119 is neither a specific nor a reliable marker for microglia. *Glia* **70**, 1170–1190 (2022).
46. Xu, F., Shen, G., Su, Z., He, Z. & Yuan, L. Glibenclamide ameliorates the disrupted blood-brain barrier in experimental intracerebral hemorrhage by inhibiting the activation of NLRP3 inflammasome. *Brain Behav.* **9**, e01254 (2019).
47. Palomino-Antolin, A. et al. Time-dependent dual effect of NLRP3 inflammasome in brain ischaemia. *Br. J. Pharmacol.* **179**, 1395–1410 (2022).
48. Franke, M. et al. The NLRP3 inflammasome drives inflammation in ischemia/reperfusion injury after transient middle cerebral artery occlusion in mice. *Brain Behav. Immun.* **92**, 223–233 (2021).
49. Michael, B. D. et al. Astrocyte- and Neuron-Derived CXCL1 Drives Neutrophil Transmigration and Blood-Brain Barrier Permeability in Viral Encephalitis. *Cell Rep.* **32**, 108150 (2020).
50. Daniels, B. P. et al. Regional astrocyte IFN signaling restricts pathogenesis during neurotropic viral infection. *J. Clin. Invest.* **127**, 843–856 (2017).
51. Jana, A. et al. Increased Type I interferon signaling and brain endothelial barrier dysfunction in an experimental model of Alzheimer's disease. *Sci. Rep.* **12**, 16488 (2022).
52. Lee, K. S. et al. Hyperglycemia enhances brain susceptibility to lipopolysaccharide-induced neuroinflammation via astrocyte reprogramming. *J. Neuroinflammation* **21**, 137 (2024).
53. Byun, D. J., Lee, J., Yu, J. W. & Hyun, Y. M. NLRP3 Exacerbate NETosis-Associated Neuroinflammation in an LPS-Induced Inflamed Brain. *Immune Netw.* **23**, e27 (2023).
54. Fernandes-Alnemri, T. et al. The AIM2 inflammasome is critical for innate immunity to Francisella tularensis. *Nat. Immunol.* **11**, 385–393 (2010).
55. Raudvere, U. et al. g:Profiler: a web server for functional enrichment analysis and conversions of gene lists (2019 update). *Nucleic Acids Res.* **47**, W191–W198 (2019).

Acknowledgements

We thank Dr. Kyoung-Ho Pyo (Yonsei University College of Medicine) for technical support regarding data analysis. We are also grateful to Dr. Ju Hee Ryu (Korea Institute of Science and Technology) for providing the caspase-1-specific probe. This work was supported by the National Research Foundation of Korea Grant funded by the Korean Government (2022R1A2C2007569 to J.W.Y., RS-2023-00207834 to J.W.Y., and 2022R1A2C10066566 to S.H.).

Author contributions

S.H.Y., E.L. and J.W.Y. conceived and designed the entire project. S.H.Y., E.L. C.L., K.S.L., B.C. and I.H. performed most of the experiments. C.K., J.K., T.G.K. and S.H. generated and analyzed scRNA-sequencing data. J.L. and Y.M.H. performed intravital imaging experiments. H.P. and J.S. performed secretome analysis by mass spectrometry. S.-H.Y., C.K., S.H. and J.W.Y. wrote the manuscript. All authors read and approved the final version of the manuscript.

Competing interests
The authors declare no competing interests.

Additional information
Supplementary information The online version contains supplementary material available at https://doi.org/10.1038/s41467-025-56097-1.

Correspondence and requests for materials should be addressed to Seunghee Hong or Je-Wook Yu.

Peer review information *Nature Communications* thanks Andrew Mendiola, Axel Montagne, Hiroaki Wake, and the other, anonymous, reviewer for their contribution to the peer review of this work. A peer review file is available.

[1]Department of Microbiology and Immunology, Brain Korea 21 Project for Medical Science, Institute for Immunology and Immunological Diseases, Yonsei University College of Medicine, Seoul, Republic of Korea. [2]Department of Biochemistry, College of Life Science and Biotechnology, Yonsei University, Seoul, Republic of Korea. [3]Department of Anatomy, Brain Korea 21 Project for Medical Science, Yonsei University College of Medicine, Seoul, Republic of Korea. [4]Doping Control Center, Korea Institute of Science and Technology, Seoul, Republic of Korea. [5]Department of Dermatology, Yonsei University College of Medicine, Seoul, Republic of Korea. [6]Present address: Division of Developmental Biology, National Institute of Child Health and Human Development, National Institute of Health, Bethesda, MD, USA. [7]These authors contributed equally: Sung-Hyun Yoon, Chae youn Kim.
✉e-mail: seungheehong@yonsei.ac.kr; jewookyu@yuhs.ac